THE

PHYSICAL REVIEW

Nuclear-Matter Radii from a Reformulated Optical Model*

G. W. GREENLEES, G. J. PYLE, AND Y. C. TANG

School of Physics, University of Minnesota, Minneapolis, Minnesota

(Received 18 January 1968)

A reformulation of the optical model is developed in which the real parts of the potential are obtained from nuclear-matter distributions and the nucleon-nucleon force. The model is applied to proton elastic scattering data at 14.5, 30.3, and 40.0 MeV and succeeds in fitting the data as well as, or better than, the standard optical model despite the fact that two fewer parameters are needed in the new model. Values, accurate to a few percent, are obtained for the nuclear rms matter radii which are independent of the incident proton energy. These values are greater than the corresponding rms proton radii obtained from electron scattering and muonic x-ray work, and indicate that nuclear neutron rms radii are greater than nuclear proton rms radii by about 0.6 F. Information is also obtained concerning the spin-isospin–independent part of the nucleon-nucleon force, indicating a mean-square radius of 2.25 ± 0.6 F^2 and a volume integral of 400 ± 20 MeV F^3. The neutron and proton density distributions found from this work and muonic studies are used to calculate the imaginary potential, and this is compared with the phenomenological form found in the analyses performed with the new model. The good measure of agreement between the two potentials indicates that the model can be extended to include this term in a more logical manner, and with fewer parameters, than in the standard formulation of the optical model. The model is readily extended, in appropriate cases, for use with complex particles.

I. INTRODUCTION

THE optical model has been used extensively in the analysis of elastic scattering data for a wide variety of particles and over a wide range of energies.[1] The present paper deals with a reformulation of the model which expresses the potential in terms of nuclear-matter distributions and the nucleon-nucleon force. The new model is used to analyze proton elastic scattering data between 14.5 and 40 MeV. As developed, the model is directly applicable to neutron scattering data and is readily extended, in appropriate cases, to heavier particles.

In the energy region below 50 MeV, extensive proton elastic scattering data exist.[1] These have, in general, been analyzed in terms of an optical model in which the interaction is represented as the scattering of a point particle (proton) by a potential of the form

$$U_{op}(r) = U_C(r) + U(r) + iW(r) + U_{so}(r) + iW_{so}(r),$$

where $U_C(r)$ is the Coulomb potential due to a uniform

distribution of appropriate size and total charge.[2] The real term $U(r)$ is almost always taken to have a volume form $-V_R f_R(r)$ with $f_R(r) = \{1+\exp[(r-R_R)/a_R]\}^{-1}$, the Woods-Saxon form factor. This real central term thus involves three parameters V_R, R_R, and a_R. The imaginary central term $W(r)$ has been taken to have a surface form, a volume form, or a mixture of surface and volume terms. Below proton energies of about 20 MeV the surface form is satisfactory and may have a Gaussian or a Woods-Saxon derivative shape. The derivative form is written as $W_s 4a_s f_s'(r)$ and contains three parameters W_s, R_s, and a_s. The volume form is correspondingly $W_v f_v(r)$ with three parameters. If both surface and volume terms are used, six parameters are involved. At proton energies above about 20 MeV, a volume term as well as a surface term seems to be necessary, but good agreement with experiment is achieved with $R_s = R_v$ $(=R_I$ say$)$ and $a_s = a_v$ $(=a_I$ say$)$, leaving four parameters W_s, W_v, R_I, and a_I for the imaginary central term. The spin-orbit term $[U_{so}(r)+iW_{so}(r)]$, is generally taken to have a Thomas

---

[1] The literature on this topic is very extensive. References 4-8 of this paper are immediately relevant to this work and they include references to other work on the subject.

[2] The predictions are not very sensitive to the details of the charge distribution used; see, for example, F. Becchetti and G. W. Greenlees, Annual Progress Report in Nuclear Physics, University of Minnesota, 1966 (unpublished).

form, with

$$U_{so}(r) = V_{so} \frac{\hbar^2}{m_\pi^2 c^2} \frac{1}{r} f_{so}'(r) \mathbf{l} \cdot \boldsymbol{\sigma}.$$

In the absence of convincing evidence to the contrary, it is usual to take $W_{so}=0$, leaving three parameters V_{so}, R_{so}, and a_{so}. The model thus involves ten parameters although several analyses have been performed using more restricted sets by equating some of the geometrical parameters and/or neglecting one of the imaginary terms.[3]

When data for a range of elements at one proton energy are analyzed, it is usual to use a set of "average" geometry parameters by taking the radii R_R, R_I, and R_{so} to vary as $A^{1/3}$ for some fixed diffuseness values. The introduction of the assumption of a specific A dependence for the radius parameters worsens the agreement between the model and experiment and in some cases, where this is particularly severe, an A dependence has been introduced for the diffuseness parameters. The advantage of such procedures is in the collation of more data in terms of a limited number of parameters and in exhibiting trends in the strength parameters with A. Such trends, however, are only significant if the basic assumptions regarding the A dependence are valid and these assumptions are not independently justified. Since R_R, R_I and R_{so} can differ by about 20–30% for a given element and projectile, a mechanism which produces the same A dependence for all three radii presents some difficulty. When data for a range of energies and elements is considered, it is usual to extend the above assumption by requiring that the average geometry be energy-independent. This exhibits trends in the strength parameters with energy. Variations of the parameters with energy are attributed to the strength rather than the geometrical parameters without any solid justification.

Thus the energy and $A(N,Z)$ dependence of the strength parameters obtained from the normal formulation of the optical model are dependent entirely upon the validity of specific geometrical assumptions which may or may not be correct. The introduction of these assumptions worsens somewhat the agreement between the model and experiment. One advantage of the formulation presented here is that these assumptions are avoided and both geometrical and strength parameter information is extracted directly from the optimum fits.

Although ten parameters are needed for an optimum fit to proton scattering data for one element at one energy, the main features of the experimental data are well represented by more restricted models. Thus Perey, in analyzing proton data at energies between 9 and 22 MeV, used a six-parameter model by choosing $W_v=0$, $R_R=R_I=R_{so}$ $(\propto A^{1/3})$, and $a_R=a_{so}$ and ob-

tained reasonable agreement with the differential cross-section data and the limited amount of polarization data then available.[4] Rosen et al. analyzed data in the energy range 7–22 MeV with similar parameter restrictions and obtained reasonable agreement with data which included extensive polarization measurements.[5] A similar treatment between 11 and 18 MeV has been given by Buck.[6]

With the availability of more extensive and higher-energy data, the parameter restrictions imposed by Perey and by Rosen et al. have been removed so that a ten-parameter model is now considered necessary unless significant compromises on the fits are to be tolerated. Although ten parameters are necessary for the best fitting of the data, ambiguities have been observed in the parameterization and it is not possible to specify a unique set of parameters even for one set of data.[7,8] Nevertheless, the over-all success of the model testifies to the basic validity of the approach. There is, however, clearly a need for a formulation more closely related to physical invariants and avoiding, if possible, the assumptions and ambiguities of the present approach.

An earlier publication used the results of a standard optical-model analysis of 30-MeV proton data to establish a connection between the real central geometry and the spin-orbit geometry via the nuclear matter distribution.[9] The present paper is a more complete treatment along these lines. The real parts of the potential (central-isospin–independent, central-isospin-dependent, and spin-orbit) are obtained from the nuclear-matter distribution and specific components of the nucleon-nucleon force. The strengths of the various components of the potential are left as adjustable parameters but the four geometrical parameters associated with the real central and spin-orbit parts of the potential in the normal formulation are replaced by two parameters associated with the matter distribution in the new model. It is thus an eight-parameter model instead of a ten-parameter model. The fits obtained with the new model are in general slightly better than those obtained with the old model despite the fact that two less parameters are being used. Well-defined values for nuclear-matter mean-square radii and the volume integrals of the real parts of the potentials are obtained for a range of $A(58–208)$ and $E(14–40$ MeV) without further assumptions. Information is also obtained concerning the nucleon-nucleon force and when nuclear-proton distributions, obtained in other experiments, are combined with the nuclear-matter information obtained here, nuclear-neutron distributions can be derived. Although the

---

[3] References 4–8 of this paper, among others.

[4] F. G. Perey, Phys. Rev. **131**, 745 (1963).
[5] L. Rosen, J. G. Beery, and A. S. Goldhaber, Ann. Phys. (N.Y.) **34**, 96 (1965).
[6] B. Buck, Phys. Rev. **130**, 712 (1963).
[7] G. R. Satchler, Nucl. Phys. **A92**, 273 (1967).
[8] G. W. Greenlees and G. J. Pyle, Phys. Rev. **149**, 836 (1966).
[9] G. W. Greenlees, G. J. Pyle, and Y. C. Tang, Phys. Rev. Letters **17**, 33 (1966).

model still contains eight parameters, there are strong indications that some of the parameters of the imaginary central term can also be eliminated.

II. MODEL

A. Formulation

In order to compute the interaction potential between the incident nucleon and the target nucleus the following approximations will be used:

(1) The incident nucleon will be treated as distinguishable; i.e., the requirement that the wave function be antisymmetrized with respect to the exchange of the incident nucleon with a nucleon in the target nucleus will be ignored.

(2) The effect of polarization of the target nucleus by the incident nucleon will not be taken into consideration.

These approximations are very likely to be valid for the present problem, since the presence of a fairly strong absorptive component in the optical potential has the consequence that the elastic scattering is sensitive mainly to the potentials in the surface region. In this latter region, it has been shown by Drell[10] that the effective potentials arising from polarization and antisymmetrization effects have rather small magnitudes.

With the above approximations, the wave function of the system can be written as

$$\Psi = \psi(\xi)\phi(\mathbf{r}_0, s_0, t_0), \tag{1}$$

where ψ is a normalized wave function describing the ground state of the target nucleus and ϕ is the scattering function. The quantity ξ denotes, collectively, the spatial, spin, and isospin coordinates of all the nucleons in the target nucleus, and $\mathbf{r}_0$, s_0, and t_0 denote the corresponding coordinates of the incident nucleon. To determine the function ϕ, a variational principle is used; i.e.,

$$\delta \int \Psi^*(H-E')\Psi dv = 0, \tag{2}$$

where E' is the total energy of the system and H is the Hamiltonian given by

$$H = H_\xi + T_0 + \sum_{i=1}^{A} u_{0i}, \tag{3}$$

with H_ξ being the Hamiltonian of the target nucleus, T_0 being the kinetic-energy operator of the incident nucleon, and u_{0i} being the two-body interaction between the incident nucleon and a nucleon i in the target nucleus. From this variational principle, one

[10] S. D. Drell, Phys. Rev. **100**, 97 (1955).

obtains

$$\int \psi^*(H-E')\Psi d\xi = 0. \tag{4}$$

Using Eqs. (1) and (4), it can be easily shown that

$$\left(T_0 + \int \psi^* \sum_{i=1}^{A} u_{0i}\psi d\xi - E_0\right)\phi = 0, \tag{5}$$

where E_0 is the energy of the incident nucleon in the c.m. system and the effective interaction potential U_0 felt by the incident nucleon is

$$U_0 = \int \psi^* \sum_{i=1}^{A} u_{0i}\psi d\xi. \tag{6}$$

In this investigation, the nucleon-nucleon potential considered is of the form

$$u_{0i} = u_d(r_{0i}) + u_\tau(r_{0i})\boldsymbol{\tau}_0 \cdot \boldsymbol{\tau}_i + u_\sigma(r_{0i})\boldsymbol{\sigma}_0 \cdot \boldsymbol{\sigma}_i$$
$$+ u_{\sigma\tau}(r_{0i})\boldsymbol{\sigma}_0 \cdot \boldsymbol{\sigma}_i\boldsymbol{\tau}_0 \cdot \boldsymbol{\tau}_i + [u_t(r_{0i}) + u_{tr}(r_{0i})\boldsymbol{\tau}_0 \cdot \boldsymbol{\tau}_i]S_{12}$$
$$+ u_{ls}(r_{0i})\frac{1}{\hbar}[(\mathbf{r}_0 - \mathbf{r}_i)\times(\mathbf{p}_0 - \mathbf{p}_i)\cdot(\boldsymbol{\sigma}_0 + \boldsymbol{\sigma}_i)], \tag{7}$$

where S_{12} is the tensor force operator. For nuclei with total angular momentum zero, the contribution to U_0 of Eq. (6) comes from the first, second, and last terms in Eq. (7). Hence

$$U_0 = U_R + U_S + U_{so}, \tag{8}$$

with

$$U_R = \int \psi^* \sum_{i=1}^{A} u_d(r_{0i})\psi d\xi, \tag{9}$$

$$U_S = \int \psi^* \sum_{i=1}^{A} u_\tau(r_{0i})\boldsymbol{\tau}_0 \cdot \boldsymbol{\tau}_i\psi d\xi, \tag{10}$$

and

$$U_{so} = \int \psi^* \sum_{i=1}^{A} u_{ls}(r_{0i})\frac{1}{\hbar}$$
$$\times[(\mathbf{r}_0 - \mathbf{r}_i)\times(\mathbf{p}_0 - \mathbf{p}_i)\cdot(\boldsymbol{\sigma}_0 + \boldsymbol{\sigma}_i)]\psi d\xi. \tag{11}$$

Using the expressions

$$\rho_p(\mathbf{r}) = \int \psi^* \sum_{i=1}^{A} \delta(\mathbf{r}_i - \mathbf{r})\tfrac{1}{2}(1+\tau_{iz})\psi d\xi, \tag{12}$$

$$\rho_n(\mathbf{r}) = \int \psi^* \sum_{i=1}^{A} \delta(\mathbf{r}_i - \mathbf{r})\tfrac{1}{2}(1-\tau_{iz})\psi d\xi, \tag{13}$$

and

$$\rho_m(\mathbf{r}) = \rho_p(\mathbf{r}) + \rho_n(\mathbf{r}) \tag{14}$$

for the proton, neutron, and matter distribution in the

target nucleus, it is straightforward to show that

$$U_R = \int \rho_m(\mathbf{r}) u_d(|\mathbf{r} - \mathbf{r}_0|) d\mathbf{r}, \tag{15}$$

$$U_S = \left\{ \int [\rho_p(\mathbf{r}) - \rho_n(\mathbf{r})] u_\tau(|\mathbf{r} - \mathbf{r}_0|) d\mathbf{r} \right\} \tau_{0z}, \tag{16}$$

and

$$U_{so} = \left\{ -\frac{1}{\hbar} \sum_{n=1}^{\infty} \frac{4\pi}{(2n+1)!} \frac{2n}{r_0} \frac{d}{dr_0} \right.$$

$$\times \left[\frac{2(n-1)}{r_0} \frac{d^{2n-3}}{dr_0^{2n-3}} \rho_m + \frac{d^{2n-2}}{dr_0^{2n-2}} \rho_m \right]$$

$$\left. \times \int_0^\infty u_{ls}(\eta) \eta^{2n+2} d\eta \right\} \mathbf{l}_0 \cdot \boldsymbol{\sigma}_0. \tag{17}$$

It should be mentioned that the right-hand side of Eq. (17) is an asymptotic series and, hence, care must be exercised in its summation.[11]

With a wave function of the form given by Eq. (1), the existence of open reaction channels is not accounted for. To take into consideration these channels in a crude manner, a phenomenological imaginary potential W will be added to the potential U_0 of Eq. (8). In this way, a potential U_{op} is obtained, which is of the type commonly used to analyze data on the scattering of nucleons by complex nuclei.

B. Preliminary Evaluation

Before proceeding with the application of the model to the analysis of proton elastic scattering data, it is worthwhile to make a preliminary evaluation to see if the consequences of Eqs. (15)–(17) are consistent with published analyses of scattering data. This is done in the present section; subsequent sections are devoted to the analysis of data using the model.

From the form of Eq. (15), it follows that

$$\langle r^2 \rangle_R = \langle r^2 \rangle_d + \langle r^2 \rangle_m, \tag{18}$$

where $\langle r^2 \rangle_R$, $\langle r^2 \rangle_d$, and $\langle r^2 \rangle_m$ are the mean square (ms) radii of the real potential U_R, the spin- and isospin-independent part u_d of the two-body potential, and the matter distribution ρ_m, respectively, and

$$J_R = A J_d, \tag{19}$$

where

$$J_R = -\int U_R(\eta) d\eta \tag{20}$$

and

$$J_d = -\int u_d(\eta) d\eta \tag{21}$$

are the volume integrals of the potentials U_R and u_d, respectively.[12]

A detailed phenomenological analysis of α-α scattering has been made by Ali and Bodmer,[13] who found that the $l=0$, 2, and 4 phases can be very well explained by using a potential which has an attractive component:

$$U_A = -V_{0A} \exp(-\mu_A^2 r^2), \tag{22}$$

with $\mu_A = 0.475$ F^{-1} and $V_{0A} = 130$ MeV. This potential has the properties that[14] $\langle r^2 \rangle_R = 6.65$ F^2 and $J_R = 6760$ MeV F^3. Using Eqs. (18) and (19) and $\langle r^2 \rangle_m = 2\langle r^2 \rangle_\alpha = 4.14 \pm 0.40$ F^2, where $\langle r^2 \rangle_\alpha$ is the ms radius of the nucleon distribution in the α particle,[15] we find

$$\langle r^2 \rangle_d = 2.51 \pm 0.40 \text{ F}^2 \tag{23}$$

and

$$J_d = 422 \text{ MeV F}^3. \tag{24}$$

This can be compared with the corresponding quantities obtained from a phenomenological nucleon-nucleon potential which has been used in a number of scattering problems involving light nuclei[16]; this potential is of the form

$$u_{ij} = -V_g \exp(-\kappa r_{ij}^2)$$
$$\times (a_d + a_\tau \boldsymbol{\tau}_i \cdot \boldsymbol{\tau}_j + a_\sigma \boldsymbol{\sigma}_i \cdot \boldsymbol{\sigma}_j + a_{\sigma\tau} \boldsymbol{\sigma}_i \cdot \boldsymbol{\sigma}_j \boldsymbol{\tau}_i \cdot \boldsymbol{\tau}_j), \tag{25}$$

with $V_g = 72.98$ MeV and $\kappa = 0.46$ F^{-2}. With a Serber exchange mixture, the constants a_d, a_τ, a_σ, and $a_{\sigma\tau}$ have the following values:

$$a_d = 0.306, \quad a_\tau = -0.148,$$
$$a_\sigma = -0.056, \quad a_{\sigma\tau} = -0.102. \tag{26}$$

This potential gives a good fit to the low-energy two-nucleon scattering data; it has

$$\langle r^2 \rangle_d = 3.26 \text{ F}^2 \tag{27}$$

and

$$J_d = 400 \text{ MeV F}^3. \tag{28}$$

Comparing these values with the values of $\langle r^2 \rangle_d$ and J_d of Eqs. (23) and (24), it is seen that there is a fairly good agreement, indicating that the relations (18) and (19) are reliable.

A second example of the reliability of Eq. (19) is obtained by using it to estimate the depth of the potential U_R. Assuming the usual form

$$U_R = -V_R\{1 + \exp[(r - R_R)/a_R]\}^{-1}, \tag{29}$$

[11] The first term $(n=1)$ in Eq. (17) has also been derived by R. J. Blin-Stoyle, Phil. Mag. 46, 973 (1955).

[12] More generally, the quantity A in Eq. (19) should be replaced by $A_t A_i$, where A_t and A_i denote the number of nucleons in the target nucleus and the incident particle, respectively.

[13] S. Ali and A. R. Bodmer, Nucl. Phys. 80, 99 (1966).

[14] Ali and Bodmer (Ref. 13) have also found another potential which fits the phase shifts equally as well. This potential has $\mu_A = 0.5$ F^{-1} and $V_{0A} = 150$ MeV. The interesting point is that, for this potential, J_R has a value of 6710 MeV F^3, which is very nearly the same as the value of 6760 MeV F^3 quoted above.

[15] R. Hofstadter, Rev. Mod. Phys. 28, 214 (1956); G. R. Burleson and H. W. Kendall, Nucl. Phys. 19, 68 (1960).

[16] Y. C. Tang, E. Schmid, and K. Wildermuth, Phys. Rev. 131, 2631 (1963); S. Okai and S. C. Park, ibid. 145, 787 (1966); D. R. Thompson and Y. C. Tang, ibid. 159, 806 (1967).

it is found that

$$J_R = V_R \tfrac{4}{3}\pi R_R{}^3 (1+\pi^2 a_R{}^2/R_R{}^2). \qquad (30)$$

Equating this with AJ_d, we obtain

$$V_R = AJ_d (3/4\pi) R_R{}^{-3} (1+\pi^2 a_R{}^2/R_R{}^2)^{-1}. \qquad (31)$$

Using $J_d = 400$ MeV F^3, $R_R = 1.20\, A^{1/3}$ F, and $a_R = 0.7$ F the values of V_R are

$$V_R = 50.4 \text{ MeV for Pb}^{208},$$
$$= 45.4 \text{ MeV for Ni}^{58}. \qquad (32)$$

From analyzing the scattering data, the phenomenological value of V_R was found to be around 45 MeV,[8] which agrees quite well with the values of Eq. (32).

For the symmetry potential U_S we note that in the special case where

$$\rho_p = Z\rho_m/A,$$
$$\rho_n = N\rho_m/A, \qquad (33)$$
$$u_\tau(r) = -\zeta u_d(r),$$

with ζ being a constant independent of r, it reduces to

$$U_S = \zeta[(N-Z)/A]\tau_{0z}U_R, \qquad (34)$$

which is of the form commonly used in optical-model analyses. The magnitude of ζ can be estimated by using the two-body potential of Eqs. (25) and (26); it is

$$\zeta = -a_\tau/a_a = 0.48, \qquad (35)$$

which does compare favorably with that found by phenomenological analyses of nucleon-nucleus scattering data.[4,8]

Under the conditions expressed by Eq. (33), information about the nucleon-nucleon potential can be extracted from the parameter values of the phenomenological optical-model potential. For the proton-nucleus case, τ_{0z} has an eigenvalue of $+1$ and (U_R+U_S) can be defined as

$$U_{RS} = U_R + U_S = U_R + [(N-Z)/A]\zeta U_R. \qquad (36)$$

Taking the volume integral of both sides and using Eq. (19), one obtains

$$-\int U_{RS}d\mathbf{r} = J_{RS} = AJ_d \left(1 + \frac{N-Z}{A}\zeta\right)$$

or $\qquad\qquad\qquad\qquad\qquad\qquad\qquad (37)$

$$J_{RS}/A = J_d + \zeta J_d (N-Z)/A.$$

Thus, by making a straight-line fit of J_{RS}/A determined from the optical-model analysis as a function of $(N-Z)/A$, one obtains the values of both J_d and ζ.

Finally, the properties of the spin-orbit potential will be discussed. At incident energies below 50 MeV it will be a good approximation to take only the first

term of Eq. (17); i.e., we can approximate U_{so} as

$$U_{so} = -\frac{1}{\hbar}\frac{4\pi}{3}\frac{1}{r_0}\frac{d\rho_m}{dr_0}\left[\int u_{ls}(\eta)\eta^4 d\eta\right]\mathbf{l}_0\cdot\boldsymbol{\sigma}_0. \qquad (38)$$

This approximation should be a reasonably valid one for the following reasons: First, the two-body spin-orbit potential is expected to be short-ranged, with $\hbar/Mc$ equal to only about 0.3 F.[17] Second, the terms with $n>1$ in Eq. (17) have a rapid variation with r_0 with a reasonable form for ρ_m, such as a Saxon-Woods form and, hence, they become important only when the incident nucleon energy is greater than about 100 MeV.

By examining Eqs. (15) and (38), it becomes immediately obvious that the form factors of U_R and U_{so} are quite different. As has been reported in a previous publication,[9] this readily explains the observation from optical-model analyses of proton scattering data[8,18,19] that the rms radius for the form factor of the spin-orbit interaction (ρ_m) is smaller than that for the form factor of the real central interaction.

If the spin-orbit potential is written in the form generally used in optical-model analyses,

$$U_{so} = \frac{V_{so}}{\hbar}\left(\frac{\hbar}{m_\pi c}\right)^2 \frac{1}{r_0}\frac{d}{dr_0}f(r_0, r_{so}, a_{so})\mathbf{l}_0\cdot\boldsymbol{\sigma}_0, \qquad (39)$$

with

$$f(r_0, r_{so}, a_{so}) = \rho_m/\rho_{m0}$$
$$= \{1 + \exp[(r - r_{so}A^{1/3})/a_{so}]\}^{-1}, \qquad (40)$$

then, by comparing with Eq. (38), one obtains

$$V_{so} = \tfrac{4}{3}\pi\rho_{m0}(\hbar/m_\pi c)^{-2}J_4, \qquad (41)$$

with

$$J_4 = -\int_0^\infty u_{ls}(\eta)\eta^4 d\eta. \qquad (42)$$

Here again, information on the two-body spin-orbit potential can be used to estimate V_{so}. The spin-orbit splitting in He^5 has been studied[20] using

$$u_{ls}(r) = -V_{ls}\exp(-\mu_{ls}r^2). \qquad (43)$$

With μ_{ls} equal to 0.27, 0.42, and 0.57 F^{-2}, the values of V_{ls} were found to be equal to 2.2, 4.9, and 8.9 MeV, respectively, while the corresponding values of J_4 are equal to 41.1, 29.2, and 24.8 MeV F^5. In this investigation a value of J_4 is needed which corresponds to a two-body spin-orbit potential of much shorter range. This can be obtained by studying the variation of J_4 with μ.

[17] R. A. Bryan and B. L. Scott, Phys. Rev. **135**, B434 (1964).
[18] J. A. R. Griffith and S. Roman, Phys. Letters **19**, 410 (1965); D. A. Lind, D. E. Heagerty, and J. G. Kelly, Bull. Am. Phys. Soc. **10**, 104 (1965); L. J. B. Goldfarb, G. W. Greenlees, and M. B. Hooper, Phys. Rev. **144**, 829 (1966).
[19] L. N. Blumberg, E. E. Gross, A. Van der Woude, A. Zucker, and R. H. Bassel, Phys. Rev. **147**, 812 (1966).
[20] Y. C. Tang, K. Wildermuth, and L. D. Pearlstein, Phys. Rev. **123**, 548 (1961).

Using the three values of J_4 mentioned above, a crude estimate of 20 MeV F^5 is obtained for J_4 in the present problem. Taking ρ_{m0} equal to 0.16 F^{-3} yields

$$V_{so} = 6.7 \text{ MeV}, \qquad (44)$$

which, again, agrees very well with the values found from phenomenological optical-model analyses.[5,7,8]

III. APPLICATION OF THE MODEL

It is seen from Eqs. (15)–(17) that if specific forms are used for ρ_p, ρ_n, u_d, u_τ, and u_{ls}, then U_R, U_S, and U_{so} can be computed without further assumption. At present, information is available concerning ρ_p, u_d, u_τ, and u_{ls}, so that an obvious procedure would be to assume suitable forms for these quantities, parametrize ρ_n, and use a search program to fit experimental data. To allow for minor corrections due to effects ignored by the model, the strength parameters V_R, V_S, and V_{so} of the folded potentials could be left adjustable. Such a procedure is entirely feasible but involves a separate numerical integration to obtain each of U_R, U_S, and U_{so} and, consequently, a relatively long computing period for each parameter iteration. Two of these integrations can be eliminated, and the model tested in a good approximation, by noting that (1) the main contribution to U_{so} comes from the first term of the series in Eq. (17), as was discussed in Sec. II B, and (2) V_S is small compared to V_R and need not be treated exactly.

In this paper, recognition of these facts is made by, first, using only the first term of Eq. (17) and, secondly, assuming that

$$\rho_p(\mathbf{r}) = Z\rho_m(\mathbf{r})/A ,$$
$$\rho_n(\mathbf{r}) = N\rho_m(\mathbf{r})/A ,$$
$$u_\tau(r) = -\zeta u_d(r) .$$

These assumptions lead to Eq. (34),

$$U_S = \zeta[(N-Z)/A]\tau_{0z}U_R ,$$

and give U_S and U_R the same volume form. This volume form for the isospin part of the potential will only occur under the assumption of identical form factors for the neutron and proton distributions. The analysis shows this assumption to be incorrect but not to the extent of materially altering the conclusions. Hence the procedure followed in this paper to obtain the effective interaction potential is:

(1) assume ρ_m has a Saxon-Woods form with parameters R_m and a_m;

(2) assume a form for u_d;

(3) obtain the form of $U_{RS}[= U_R[1+((N-Z)/A)\zeta]]$ from folding of ρ_m and u_d [Eq. (15)], leaving the coefficient V_{RS} of U_{RS} as a strength parameter;

(4) take only the first term of Eq. (17), giving

$$U_{so} \propto \frac{1}{r_0} \frac{d\rho_m}{dr_0} \mathbf{l}_0 \cdot \boldsymbol{\sigma}_0 ,$$

with the coefficient V_{so} as a strength parameter, and

(5) introduce an imaginary potential with both surface and volume components.

The form used for u_d is to be obtained from analysis of two-body data. Many such analyses have been made yielding mean-square radii (msr) for u_d in the range 1.5 to 3.5 F^2. Theoretically, this term is often attributed to a 2π exchange mechanism which, with a Yukawa shape, has a msr of 3 F^2 in agreement with the results of phenomenological analyses.[21] In the present paper a Yukawa form is used which enables Eq. (15) to be reduced to a one-dimensional integral. Initially a range corresponding to a 2π exchange force is used, and in Sec. IV B the sensitivity of the model to this range is explored. Phenomenological analyses of two-body data, which include high-energy results, require a repulsive core for the potential. In this analysis, however, the use of a purely attractive potential should be appropriate since, in the energy range being considered, the presence of an absorptive component in the optical potential has the consequence that the nucleon-nucleus scattering data are sensitive mainly to the tail region of the real central potential and, for this latter region, the contribution comes predominantly from the long-range part of the potential u_d.[10] At higher energies, on the other hand, repulsive core effects may well become important and will place an upper limit of about 100 MeV on the model.

The interaction potential used can be written as[22]

$$U_{op}(r) = U_C(r) - V_{RS}I(r)/I(0) - iW_vf_I(r)$$
$$+ iW_s 4a_I[df_I(r)/dr] + V_{so}(\hbar/m_\pi c)^2$$
$$\times (1/r)[df_m(r)/dr]\mathbf{l}\cdot\boldsymbol{\sigma}, \qquad (45)$$

where

$$U_C(r) = (Ze^2/2R_c)[3-(r/R_c)^2], \quad r \leqslant R_c$$
$$= Ze^2/r, \qquad\qquad\qquad r \geqslant R_c$$

is the Coulomb potential between a nucleon of charge e and a uniformly charged sphere of radius $R_c = 1.2A^{1/3}$ F. Also,

$$I(r) = \int f_m(\boldsymbol{\eta})f_d(|\boldsymbol{\eta}-\mathbf{r}|)d\boldsymbol{\eta} ,$$

with

$$f_d(r) = \exp(-\mu r)/\mu r$$

---

[21] The longer-range components of the force are associated with terms in Eq. (7) which do not contribute to the interaction potential in first order.

[22] The spin-orbit term of Eq. (45) differs from that given in Eq. (39) by a factor $\hbar^{-1}$. Equation (45) conforms to convention with l having the magnitude of the angular-momentum quantum number. In Eq. (39), l_0 [which is l of Eq. (45)] is the angular momentum itself and was used to make Sec. II consistent.

and

$$f_m(r) = \rho_m(r)/\rho_{m0} = [1+\exp((r-R_m)/a_m)]^{-1},$$

$$f_I(r) = [1+\exp((r-R_I)/a_I)]^{-1}.$$

In this expression for $U_{op}(r)$ the suffix zero has been dropped from r_0, l_0, and σ_0. This procedure will be retained for the remainder of this paper.

Subsequent parts of Sec. III B give details of the fitting procedures followed in the application of the model to proton data. The results of this section of the work are summarized in Figs. 2-7 and Tables III-VI.

The performance of the model has been tested by analyzing existing proton elastic scattering data using the potential of Eq. (45). A minimum requirement for such data is that corresponding differential cross-section and polarization measurements should be available. Data at three energies were considered suitable; these are data at 14.5, 30.3, and 40 MeV. At 14.5 MeV the differential cross-section data of Lind et al.[23] were used together with the polarization data of Rosen et al.[5]; at 30 MeV the Rutherford Laboratory data were used[24-26]; and at 40 MeV the Oak Ridge data were used.[19] In all cases the quoted errors for the experimental points were taken as being the best estimate available of the accuracy. A more convenient error treatment, from the computational viewpoint, is to use a constant percentage error at all angles for a given element; it was felt that such a procedure was not justified in the present case since it must necessarily obscure some of the information present in the data. The polarization data had in all cases been obtained using an angular acceptance sufficiently large to introduce some experimental averaging into the measurements. This makes the experimental polarization curve somewhat different from that which would be obtained using an angular acceptance small compared to the width of the angular oscillations in the data. The model predictions for polarization were therefore averaged over the angular acceptance used in the experiment, before a comparison was made with the data in the search routine. This 'smearing' of the predictions was obtained from the expression

$$\bar{P}(\theta) = \left[\int_{\theta-\frac{1}{2}\Delta\theta}^{\theta+\frac{1}{2}\Delta\theta} \sigma(\theta')d\theta'\right]^{-1} \int_{\theta-\frac{1}{2}\Delta\theta}^{\theta+\frac{1}{2}\Delta\theta} \sigma(\theta')P(\theta')d\theta',$$

where $\Delta\theta$ is the experimental angular acceptance which includes a contribution from both the detector aperture and the finite target beam spot.

[23] D. A. Lind et al. (private communication).
[24] B. W. Ridley and J. F. Turner, Nucl. Phys. 58, 497 (1964).
[25] J. F. Turner, B. W. Ridley, P. F. Cavanagh, G. A. Gard, and A. G. Hardacre, Nucl. Phys. 58, 509 (1964).
[26] R. M. Craig, J. C. Dore, G. W. Greenlees, J. S. Lilley, J. Lowe, and P. C. Rowe, Nucl. Phys. 58, 515 (1964).

A numerical comparison of the predictions of the model and the data was obtained in the usual manner from the X^2 criterion, where X^2 is defined by

$$X^2 = \frac{1}{N}\sum_{i=1}^{N}\left[\frac{q_{th}(\theta_i)-q_{expt}(\theta_i)}{q_{error}(\theta_i)}\right]^2,$$

where $q_{th}(\theta_i)$ and $q_{expt}(\theta_i)$ are the theoretical and experimental quantities at scattering angle θ_i, respectively, and $q_{error}(\theta_i)$, is the associated experimental error. The parameters of the model were varied, using a search procedure to find a minimum in X^2.

The data at 30.3 MeV[24-26] were considered to be the most detailed and accurate of the three sets considered (14.5, 30.3, and 40 MeV). In addition, this data has been extensively analyzed using the conventional optical model,[7,8,27] thus facilitating a comparison with the present model. For these reasons, most attention was paid to the 30.3-MeV data and the results of the study applied to the 14.5- and 40-MeV data.

A. Analysis of 30.3-MeV Data

Differential cross sections[24] and polarization data[26] were available for Ca^{40}, Ni^{58}, Co^{59}, Ni^{60}, Sn^{120}, and Pb^{208}. The cross-section data in general covers an angular range of 4° to 160° in 2° intervals and has an accuracy of 1 to 4% except for a few forward and backward angles. The polarization data spans the angular range 20-120° in 5° intervals with an absolute accuracy of 0.02-0.03, except at large angles. Thus approximately 80 cross-section and 20 polarization points were available for each of six elements. It was felt that to include all of these data points in the fitting procedure would give too much weighting to the cross-section measurements at the expense of the polarization results and that this might result in an insensitivity to the quality of the polarization fits. For this reason, only half of the cross-section points were used covering the angular region 4°-160° in 4° steps. The smoothness of the experimental cross-section angular distributions ensures that this procedure will not materially affect the cross-section fitting.

Three analyses of these data have been performed, using the standard optical model,[7,8,27] and in each case the fits found for Ca^{40} were relatively unsatisfactory. It was noted in an earlier paper by the present authors[9] that the optical-model parameters found for Ca^{40} in a standard optical-model analysis did not show the features found with the other elements at 30 MeV. Since these features have been incorporated in the

[27] P. E. Hodgson, R. G. Barrett, and A. Hill, Nucl. Phys. 62, 133 (1965).

present model, Ca^{40} was excluded from the initial study.[28]

This section, therefore, presents the analysis of 30.3-MeV proton elastic scattering data for Ni^{58}, Co^{59}, Ni^{60}, Sn^{120}, and Pb^{208}.[29] For each element approximately 40 cross-section points between 4 and 160° and 20 polarization points between 20 and 120° were used. The experimental reaction cross section was also available for each element[25] but this single data point was not included in the search procedure.

A difficulty arose because the energy at which the cross-section and polarization data were taken differed by approximately 1 MeV. The differential cross sections were for an energy of 30.3 MeV and the polarization data for 29.0 MeV. The difference is due to the thicker targets needed in the polarization measurements. Greenlees and Pyle, in a conventional optical-model analysis,[8] used an energy of 29.5 MeV for both the cross-section and the polarization data. However, Satchler,[7] in a similar analysis, compared the parameters obtained using 29.5 MeV for all the data with those obtained using the cross sections only at the correct energy (30.3 MeV). The differences in the parameters found by Satchler were negligible for the medium-weight elements, but were noticeable for Pb^{208}. In the present work, using the new model, a comparison has been made between the results using both schemes: (1) analyzing cross-section and polarization data using an energy of 29.5 MeV, and (2) analyzing cross-section data only at 30.3 MeV.

The model has four strength parameters V_{RS}, W_v, W_s, and V_{so} and four geometrical parameters R_m, a_m, R_I, and a_I. It was not possible, in general, to search on all eight parameters simultaneously and obtain a converged minimum in χ^2. The principal difficulty was associated with parametrization of the imaginary central potential where ambiguities exist. Two groups of six parameters were used which in most cases could be searched on simultaneously to yield a converged minimum. These groups were: (1) V_{RS}, W_v, W_s, R_I, R_m, and V_{so}, and (2) V_{RS}, W_v, W_s, a_I, a_m, and V_{so}. If the search is commenced with group (1), a_I is initially

fixed. Following the search on group (1) with a search using group (2), when a_I is varied, may not produce any very appreciable change in a_I and the search, in some cases, has been limited to a restricted region of parameter space by the initial choice of a_I. Starting with a different a_I can produce a different χ^2 minimum and a different set of imaginary parameters. The procedure used, in general, was to search on parameter groups (1) and (2) cyclically until the χ^2 converged and to check that the best minimum had been obtained by repeating the process a few times using different starting parameters. In one case (Ni^{58}) this procedure did not prove satisfactory and each different set of starting parameters gave a different minimum in parameter space, making it impossible to be sure that the best minimum had been found. The procedure used in this case (Ni^{58}) was to perform a double grid on W_v and a_I. Thus, for a fixed W_v, searches were performed on the other parameters for a range of fixed values of a_I, and this procedure was repeated for a range of values of W_v. The results of these double grids for Ni^{58} are given in Fig.1. In this figure, part (a) gives the results of searches on the cross-section and polarization data at 29.5 MeV, and part (b) gives the results using cross-section data only at 30.3 MeV. Each point plotted on Fig. 1 represents a converged χ^2 minimum for the variation of V_{RS}, W_s, V_{so}, R_m, a_m, and R_I for the appropriate values of W_v and a_I. This figure clearly shows that a number of local minima exist for a range of values of a_I and a range of values of W_v. The a_I and W_v values for the lowest minima in Fig. 1 were chosen as starting
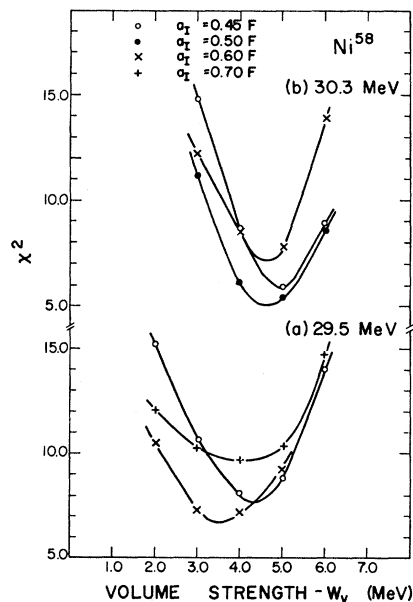
[28] Several optical-model analyses of Ca data have been performed and, in all cases, the agreement between the model and experiment has been relatively unsatisfactory. The reason for this is not clear. It is possible that for a nucleus as light as Ca, the antisymmetrization effect cannot be neglected and, hence, the use of a purely attractive real central potential in these analyses is not justified. In fact, it was found in the analysis of the α-α scattering data that the experimentally determined phase shifts can only be reproduced with the introduction of a repulsive component in the phenomenological potential. Thus, it would indeed be interesting to see if such a modification can also improve the results of the Ca analysis. Although Ca data were not included in the analysis given here, the fits obtained for the 30-MeV Ca^{40} data, using the results of the analyses, produce χ^2 values equally as good as those obtained in standard optical-model analyses (Refs. 7, 8, and 27).

[29] The spin of Co^{59} is nonzero so that, strictly speaking, the model cannot be used in this case. However, with a mass number as high as 59, it was felt that no serious error would be involved in the use of the model and it is of interest to confirm this view.

FIG. 1. Plots of best-fit χ^2 values for Ni^{58} as a function of the imaginary volume strength (W_v) for various values of the imaginary diffuseness (a_I). (a) Used cross-section and polarization data at a mean energy of 29.5 MeV; (b) used cross-section data only, at 30.3 MeV.

TABLE I. Best-fit parameter sets obtained (1) using cross-section[a] and polarization data[b] and an energy of 29.5 MeV, and (2) using cross-section data[a] only at 30.3 MeV.

Element	Ni[58]		Co[59]		Ni[60]		Sn[120]		Pb[208]	
Energy (MeV)	29.5	30.3	29.5	30.3	29.5	30.3	29.5	30.3	29.5	30.3
V_{RS} (MeV)	53.95	53.99	56.02	54.69	53.08	54.04	52.88	52.87	57.46	56.07
W_v (MeV)	4.15	4.69	3.40	4.13	3.46	4.08	3.00	3.43	2.14	2.61
W_s (MeV)	3.90	3.44	4.80	4.31	5.02	4.37	7.83	7.18	8.13	7.79
r_I (F)	1.385	1.396	1.350	1.352	1.328	1.350	1.351	1.351	1.355	1.332
a_I (F)	0.549	0.492	0.622	0.583	0.611	0.579	0.600	0.605	0.777	0.751
V_{so} (MeV)	5.53	5.16	6.12	5.67	5.65	5.31	5.84	5.61	5.43	5.16
r_m (F)	1.149	1.147	1.129	1.150	1.170	1.154	1.188	1.188	1.153	1.176
a_m (F)	0.592	0.575	0.603	0.560	0.571	0.569	0.630	0.528	0.611	0.489
χ_σ^2	5.3	5.0	5.4	5.6	5.1	4.5	3.8	3.2	1.8	1.0
χ_p^2	5.9	...	10.1	...	17.1	...	7.4	...	3.7	...
χ_T^2	5.5		7.2		9.2		4.9		2.5	

[a] Reference 24.
[b] Reference 26.

values, and parameter groups (1) and (2) were varied successively to yield a rapid convergence on the optimum χ^2 fit. This procedure for Ni[58] involved very lengthy computing periods and it was not practicable to apply this treatment to all elements. Fortunately Ni[58], at 30 MeV, was the only case where it appeared to be necessary.

Table I gives the best-fit parameter sets obtained for all the elements using both 29.5 MeV with cross-section and polarization data and 30.3 MeV with only cross-section data. The radius parameters in Table I and in all sebsequent parts of this paper are quoted as $r = R/A^{1/3}$. This conforms to convention and makes a comparison between different elements easier; however, this is only for convenience and no assumptions are made in this paper concerning the A dependence of nuclear radii. The quality of the fits as measured by the cross-section χ^2 values (χ_σ^2) are not appreciably different for the two procedures, except in the case of Pb[208], although, in general, the 30.3-MeV values are slightly lower. For Pb[208] the improvement in χ_σ^2 using 30.3 MeV is a factor of nearly 2 and is just discernable on visual inspection. The parameter values found using the two energies show little variation for Ni[58], Co[59], and Ni[60]. However, with Sn[120] and Pb[208] a significant difference in the matter diffuseness a_m is obtained with these two treatments.

The 30.3-MeV treatment using cross-section data only, at the energy for which it was measured, is undoubtedly a more correct analysis of this part of the data but raises the question as to the validity of obtaining a matter geometry (R_m and a_m) that determines the form factor for both the spin-orbit and the real potential without using the restrictions imposed by the polarization data. In other words, the improvement in χ_σ^2 obtained using the 30.3-MeV procedure and only cross-section data could be due simply to using the same number of parameters to fit less data. The parameters determined at 30.3 MeV were therefore used to fit the polarization data at 29 MeV. Experience with normal optical-model analyses indicates that the geometries and the spin-orbit strength are relatively insensitive to

the proton energy, but that the strength parameters for the central potential show an energy dependence. It is therefore reasonable to expect a fit to the polarization data at 29.0 MeV using the 30.3-MeV parameters with small changes in V_{RS}, W_s, and W_v. When a fit was obtained to the polarization data by searching on these three parameters, appreciable changes of V_{RS}, W_s, and W_v were found, changes which were inconsistent with the energy dependence of the model parameters determined over the energy range 14–40 MeV and given in Sec. V B. The comparison between the model and the polarization data at 29 MeV was therefore obtained by making fixed changes to some, or all, of V_{RS}, W_s, and W_v and comparing the predictions with experiment. The energy dependence of V_{RS} for constant geometry was estimated using the results of Sec. V B and the central strength found at 30.3 MeV was increased by 0.5 MeV for use at 29.0 MeV. The corresponding changes in W_v and W_s were estimated from Table I, which gives calculations at 29.5 and 30.3 MeV. Two procedures were used to fit the polarization data at 29 MeV, yielding parameter sets A and B. Parameter set A is identical with those given in Table I for 30.3 MeV except that V_{RS} is increased by 0.5 MeV. For parameter set B, V_{RS} is increased by 0.5 MeV, W_v is decreased by 0.8 MeV, and W_s is increased by 0.8 MeV. Table II compares the polarization χ^2 values (χ_p^2) obtained using the 29.5-MeV procedure with that using sets A and B at 29.0 MeV. In general, set A

TABLE II. Comparison of polarization χ^2 values (χ_p^2) obtained (1) using average energy and fitting cross-section and polarization data simultaneously, and (2) using parameters obtained from fitting cross-section data only at 30.3 MeV, adjusted for use at the energy of the polarization data (29 MeV). Two different adjustment procedures were used (A and B, see text).

Element	29.5 MeV	Polarization χ^2 29.0 MeV (A)	29.0 MeV (B)
Ni[58]	5.9	6.3	5.2
Co[59]	10.1	9.1	9.1
Ni[60]	17.1	15.4	14.6
Sn[120]	7.4	5.4	5.1
Pb[208]	3.7	4.0	3.3

TABLE III. Best-fit parameter sets for the 30-MeV data using the procedure outlined in text. The polarization χ^2 values (*) are obtained by adjustment of the parameters given in this table, as outlined for sets B (see text).

Element	Ni58	Co59	Ni60	Sn120	Pb208
V_{RS} (MeV)	53.95	54.69	54.04	52.87	56.07
W_v (MeV)	4.69	4.13	4.08	3.43	2.61
W_s (MeV)	3.44	4.31	4.37	7.18	7.79
r_I (F)	1.396	1.352	1.350	1.351	1.332
a_I (F)	0.492	0.583	0.579	0.605	0.751
V_{so} (MeV)	5.16	5.67	5.31	5.61	5.16
r_m (F)	1.147	1.150	1.154	1.188	1.176
a_m (F)	0.575	0.560	0.569	0.528	0.489
χ_σ^2	5.0	5.6	4.5	3.2	1.0
χ_p^2	5.2*	9.1*	14.6*	5.1*	3.3*
σ_R (mb)	1089	1157	1161	1657	2047
σ_R (expt)(mb)	1038±43	1169±39	1053±51	1638±68	1865±98

produces polarization fits just as good as obtained at 29.5 MeV and set B shows a 10–20% improvement in χ_p^2. This, therefore, justifies the parameter sets obtained from the cross-section data only at 30.3 MeV and these are taken as being the optimum sets. Table III lists these best-fit parameters for all cases at 30.3 MeV and compares the predicted and experimental reaction cross sections. The χ_p^2 values listed in Table III are obtained using the procedure outlined for the set B parameters. The corresponding curves together with the experimental points are given in Figs. 2 and 3.

B. Analysis of 14.5- and 40-MeV Data

At 40 MeV suitable data exist for Ni58, Zr90, and Pb208 [19] whereas at 14.5 MeV, data for a wide range of
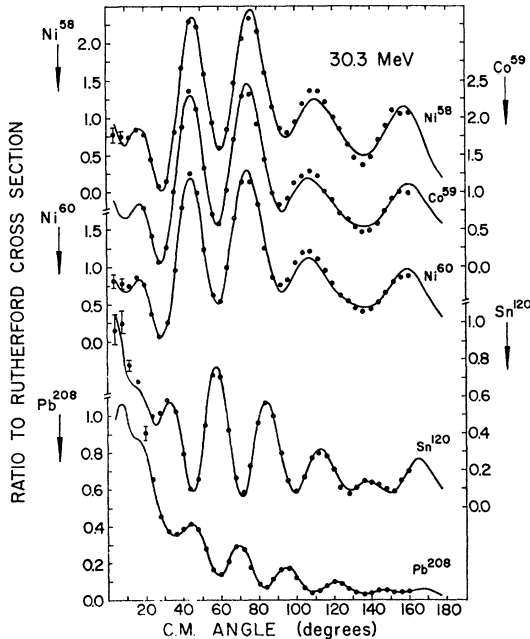
FIG. 2. Fits to 30.3-MeV cross-section data for various elements. Solid lines are the model predictions, the points are the data of Ridley and Turner (Ref. 24). Where error bars are not shown they are less than the size of the points.
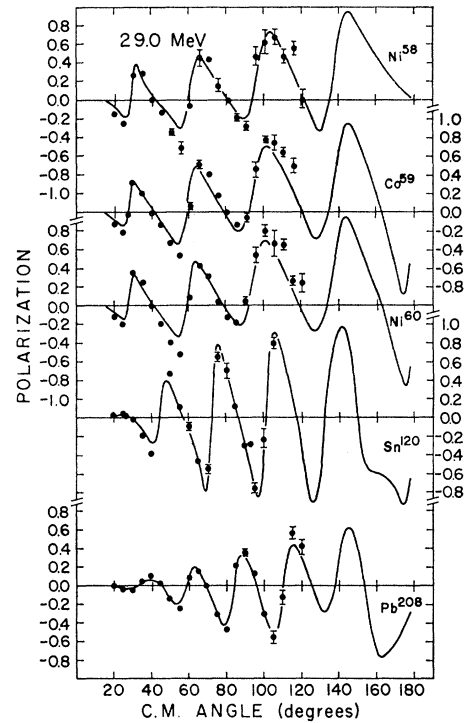
FIG. 3. Fits to 29.0-MeV polarization data for various elements. Solid lines are the model predictions; the points are the data of Craig et al. (Ref. 26). The model predictions were obtained by correcting the parameters obtained in the 30.3-MeV cross-section analysis for the energy change (see text). Where error bars are not shown they are less than the size of the points.

elements are available.[5,23] Since the purpose of the present work was to examine the performance of the model, rather than undertake an analysis of all possible data, the elements chosen for initial study at 14.5 MeV were those common with the elements at one or both of the energies 30 and 40 MeV. Four sets of 14.5-MeV data fall into this category; these are the data for Ni58, Ni60, Zr90, and Sn120.

At 40 MeV the data for each element consisted of about 60 differential cross-section points between 10° and 170°, with accuracies ranging from 1 to 15% and

TABLE IV. Best-fit parameter sets for 14.5- and 40-MeV data.[a] W_v was set equal to zero for the 14.5-MeV studies.

Element	Ni58	Ni60	Zr90	Sn120	Ni58	Zr90	Pb208
Energy (MeV)	14.5	14.5	14.5	14.5	40.0	40.0	40.0
V_{RS} (MeV)	55.22	53.08	52.74	57.15	51.53	52.50	56.67
W_v (MeV)	...	...	...	...	5.64	5.54	5.61
W_s (MeV)	7.59	10.96	7.07	10.01	2.16	3.60	4.27
r_I (F)	1.344	1.339	1.374	1.280	1.410	1.379	1.458
a_I (F)	0.644	0.503	0.659	0.672	0.520	0.510	0.587
V_{so} (MeV)	6.55	7.27	6.70	6.55	6.07	4.85	5.09
r_m (F)	1.189	1.221	1.243	1.203	1.116	1.158	1.118
a_m (F)	0.442	0.511	0.436	0.494	0.613	0.572	0.716
χ_σ^2	4.0	4.2	3.5	1.1	8.0	26.0	27.7
χ_p^2	6.4	5.1	3.4	2.4	30.5	18.7	6.1
χ_T^2	4.9	4.5	3.5	1.5	15.1	24.0	20.7

[a] References 5, 19, and 23.

increasing with angle, together with about 30 polariza-
tion values with absolute accuracies ranging from
0.07 to 0.15. At 14.5 MeV about 30 differential cross-
section points were available between 20° and 170° for
each element with accuracies of 3–4% together with the
same number of polarization points in the angular
range 30°–170° with absolute accuracies ranging from
about 0.05 to 0.08 and increasing with angle.

The polarization and cross-section data at both 14.5
and 40 MeV were taken at the same proton energy en-
abling both pieces of information to be used simul-
taneously in the search procedure. This was done using
the method outlined for 30.3 MeV and the best-fit
parameters together with the X^2 values found are given
in Table IV. The corresponding angular distributions
and experimental points are given in Figs. 4–7. In the
14.5-MeV analysis a pure surface form was used for
$W(W_v=0)$; such a procedure is normally followed in
standard optical-model analyses at this energy since
the inclusion of a volume component does not improve
the quality of the fits obtained.

C. Comparison with Other Analyses of the Data

1. 30.3-MeV Data

The 30.3-MeV data has been extensively analysed
using the standard optical model[7,8,27] and it is the data
to which most attention has been paid in the present
analysis; it therefore represents the best basis upon

FIG. 5. Fits to 14.5-MeV polarization data for various elements.
Solid lines are the model predictions; the points are the data of
Rosen et al. (Ref. 5). Where error bars are not shown they are
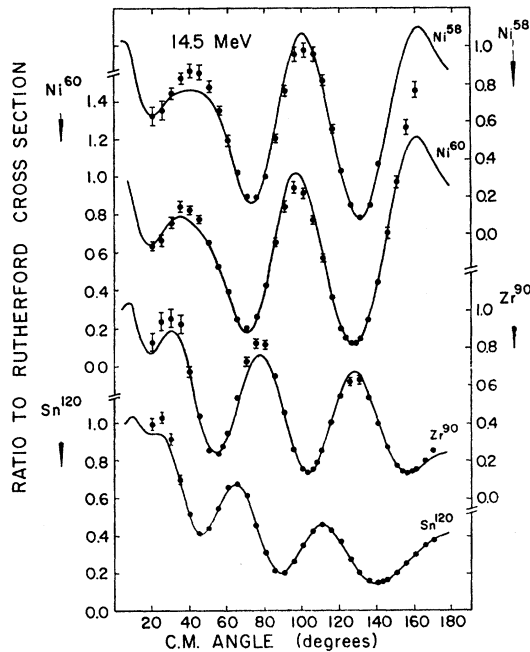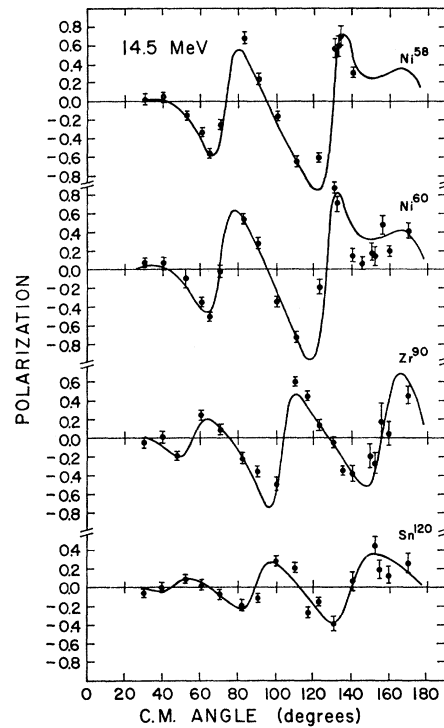less than the size of the points.

FIG. 4. Fits to 14.5-MeV cross-section data for various elements.
Solid lines are the model predictions; the points are the data of
Lind et al. (Ref. 23). Where error bars are not shown they are less
then the size of the points. Data at angles greater than 140°
for Ni⁵⁸ were not included in the fitting procedure since a com-
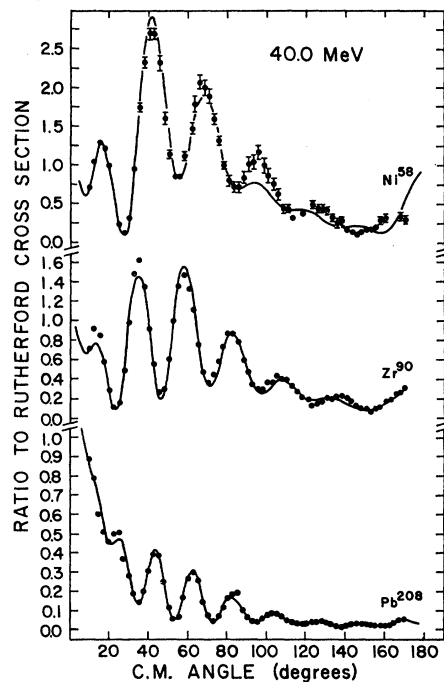pound elastic contribution was thought to be present.

FIG. 6. Fits to 40.0-MeV cross-section data for various elements.
Solid lines are the model predictions; the points are the data of
Blumberg et al. (Ref. 19). Where error bars are not shown they
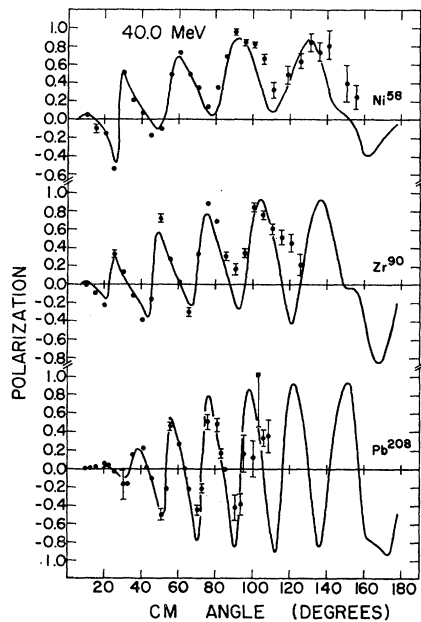are less than the size of the points.

Fig. 7. Fits to 40.0-MeV polarization data for various elements. Solid lines are the model predictions; the points are the data of Blumberg *et al.* (Ref. 19). Where error bars are not shown they are less than the size of the points.

which to compare the two models. The difficulties occasioned by the cross-section and polarization data being for different incident energies were resolved by using the cross-section data only for the corresponding energy, 30.3-MeV, and adjusting the parameters to allow for the energy change before making a comparison with the polarization data at 29.0 MeV. A similar procedure was used by Satchler for these data using a standard 10-parameter model.[7] Table V compares the cross-section χ^2 values obtained using Satchler's parameters and the standard optical model with the present results of Table III.

It is seen from Table V that somewhat better χ^2 values are obtained with the present model despite the fact that two less adjustable parameters are being used. This provides a good justification of the present approach and implies that the real-potential shape, obtained here from the folding procedure, is more satis-

TABLE V. Comparison of the χ^2 values obtained for the 30.3-MeV differential cross-section data[a] using (1) Satchler's parameters[b] obtained with a 10-parameter standard optical-model analysis, and (2) the present 8-parameter model. The χ^2 values given in (1) may differ slightly from those quoted by Satchler since he used a constant fractional error for all points whereas, in the present work, the quoted experimental errors were used.

Element	Ni[58]	Co[59]	Ni[60]	Sn[120]	Pb[208]
10-parameter model	5.51	5.72	5.40	4.07	1.13
8-parameter model	4.98	5.59	4.50	3.21	0.95

[a] Reference 24.
[b] Reference 7.

factory than the usual Saxon-Woods shape of the standard formulation.

2. *14.5- and 40-MeV Data*

A similar comparison to the one given above for the 30.3-MeV data was not possible in the case of the 14.5-MeV data, since no standard optical-model analysis has been published for the cross-section and the polarization data together. However, the χ^2 values of Table IV together with Figs. 4 and 5 indicate clearly that the data are being well reproduced in the present work.

The 40-MeV data used here are published together with a standard optical-model analysis so that the comparison can be made. This is done in Table VI. Both analyses give χ^2's appreciably greater then those found at the other two energies examined but are similar in their ability to represent the data.[30]

IV. INVESTIGATION OF THE MODEL

A. Matter Parameters

It is seen in the previous two sections that the model produces good fits to experimental proton elastic data

TABLE VI. Comparison of the χ^2 values obtained for the 40-MeV differential cross-section and polarization data using (1) the parameters of Blumberg *et al.*[a] with a 10-parameter standard optical-model analysis, and (2) the present 8-parameter model.

Element	Ni[58]	Zr[90]	Pb[208]
10-parameter model	12.0	18.0	64.1
8-parameter model	15.1	24.0	20.7

[a] Reference 19.

in the energy range 14.5–40 MeV. As proposed, the model parameters are directly related to nuclear-matter distributions. It is to be expected that the detail that may be obtained concerning nuclear-matter distributions will be limited by the accuracy of the data, the averaging effects due to the finite proton wavelength ($\lambda \approx 1$ F), and the simplifying assumptions of the model. Analyses of electron scattering by nuclei indicate that the mean-square radius of the nuclear-charge distribution is the feature most readily determined rather than details such as the half-density radius and the edge falloff distance.[31] Thus the R_m and a_m of the present Saxon-Woods parametrization of the matter distribution may be less well defined than the matter mean-square radius $\langle r^2 \rangle_m$. In order to explore this, the data for each element were fitted for a range of fixed values of a_m by searching on all other parameters including R_m. This

[30] Subsequent to this section of the work being completed, the 40-MeV data has been corrected slightly and reanalyzed with the standard optical model [M. P. Fricke *et al.*, Phys. Rev. **156**, 1207 (1967)].

[31] B. Hahn, D. G. Ravenhall, and R. Hofstadter, Phys. Rev. **107**, 1131 (1956).

gridding on a_m was performed for all cases at the three energies. The parameter sets obtained for Ni^{60} at 30.3 MeV for a_m ranging from 0.45 to 0.70 F in steps of 0.05 F are given in Table VII together with the rms radii for the matter distribution and the minimum X_σ^2 values found. Table VII clearly demonstrates the constancy of the rms radii for wide variations of R_m and a_m and a range of a factor 3 in the minimum X_σ^2 values. This implies that for any value of a_m within a wide range, obtaining a X^2 minimum determines the rms matter radius very well even though the fit obtained may be far from optimum. The same feature was found for all cases and the data are summarized in Table VIII. In this table the expression ΔY corresponding to a quantity Y is defined as $100\times(Y_{max}-Y_{min})/(Y_{max}+Y_{min})$ and gives a measure of the variation of Y in the range explored. The variation found for the rms matter radii are, in all cases, much smaller than the variations in R_m, a_m, and X_σ^2, generally an order of magnitude smaller. Table VIII clearly demonstrates

TABLE VII. Optimum parameter sets for a range of values of the matter diffuseness (a_m) for the scattering of 30.3-MeV protons by Ni^{60}.

V_{RS} (MeV)	48.64	50.92	52.90	55.52	58.29	61.07
W_v (MeV)	3.72	3.76	4.09	4.12	3.83	3.42
W_s (MeV)	5.27	5.27	4.51	4.06	4.08	4.36
r_I (F)	1.303	1.304	1.339	1.376	1.399	1.412
a_I (F)	0.576	0.571	0.577	0.579	0.582	0.588
V_{so} (MeV)	6.25	5.49	5.27	5.45	5.96	6.67
r_m (F)	1.237	1.204	1.170	1.130	1.087	1.041
a_m (F)	0.45	0.50	0.55	0.60	0.65	0.70
$\langle r^2\rangle_m^{1/2}$ (F)	4.105	4.097	4.094	4.088	4.086	4.092
X_σ^2	14.50	7.91	4.77	4.99	7.44	10.72

that $\langle r^2\rangle_m$, as defined in the model, is well determined independent of the details of the search routine and fitting procedure.

The variation of X_σ^2 with a_m for Ni^{60} at 30.3 MeV (Table VII) is plotted in Fig. 8. The width of this curve can be used to estimate the range of values of a_m and R_m which will produce acceptable fits to the data. The plots of the data and the predictions for the various a_m values were examined to determine when the fit obtained became visibly worse than the optimum. In this way it was empirically determined that an increase of X_σ^2 by a factor of 1.5 was noticeable. The factor 1.5 was found to be reasonable for all the medium-weight elements whereas for the heavy elements a factor 2.0 in X_σ^2 was needed before the fit became visibly worse. The variations allowed in r_m and a_m are, of course, not independent since, for a given a_m, r_m is such as to keep the ms radius $\langle r^2\rangle_m$ nearly constant, where

$$\langle r^2\rangle_m = \tfrac{3}{5}R_m^2[1+(7/3)(\pi a_m/R_m)^2] \quad \text{with} \quad R_m = r_m A^{1/3}.$$

In order to obtain an error for the rms radius determined by these fits, it is strictly necessary to obtain

TABLE VIII. Summary of the results of a_m grid studies for all cases considered. The entry ΔY of a quantity Y is defined as $100(Y_{max}-Y_{min})/(Y_{max}+Y_{min})$.

Element	Energy (MeV)	Δr_m	Δa_m	ΔX^2	$\Delta\langle r^2\rangle_m^{1/2}$
Ni^{58}	14.5	9.4	40.0	34.7	0.35
Ni^{58}	30.3	10.4	21.7	19.4	1.22
Ni^{58}	40.0	12.3	28.0	36.5	1.50
Co^{59}	30.3	9.2	21.7	46.1	0.45
Ni^{60}	14.5	6.9	33.3	45.4	0.43
Ni^{60}	30.3	8.6	21.7	50.5	0.23
Zr^{90}	14.5	9.5	33.3	70.6	1.88
Zr^{90}	40.0	6.7	21.7	15.5	0.59
Sn^{120}	14.5	3.9	33.3	43.0	0.27
Sn^{120}	30.3	5.5	33.3	41.5	0.58
Pb^{208}	30.3	5.7	33.3	51.8	1.78
Pb^{208}	40.0	7.5	30.8	35.4	0.98

contour plots of constant X^2 values for variations of r_m and a_m. The range of rms radii allowed by the contour with X^2 equal to 1.5 (medium A) and 2.0 (heavy A) times the optimum gives a measure of the error involved. Such contour plots are given for Ni^{58} and Pb^{208} at 30 MeV in Fig. 9, where it is seen that variations of 10–15% in r_m and about 50% in a_m are possible for visibly equivalent fits. Lines of constant rms radius are also shown in Fig. 9 and are seen to run closely parallel to the lines of constant X^2. The contours shown are for $X^2=1.5X_{opt}^2$ for Ni^{58}, and $X^2=2.0X_{opt}^2$ for Pb^{208}, so that any values of r_m and a_m enclosed by these curves yield acceptable fits. For the other cases examined, full contour plots were not obtained since this was too time consuming. In these cases plots of X^2 against rms radius were obtained for corresponding values of r_m and a_m moving along a line perpendicular to lines of constant rms radius and passing through the best-fit values. The width of such curves readily yields
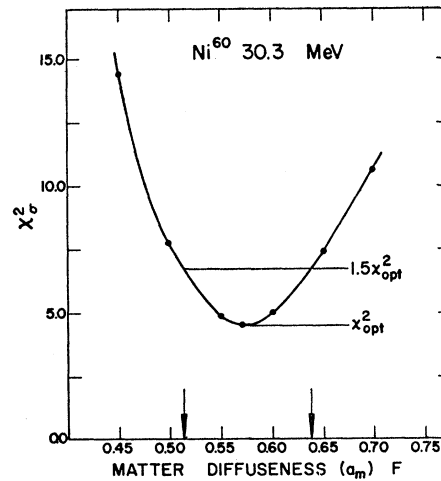

FIG. 8. Variation of best-fit X_σ^2 with the matter diffuseness (a_m) for Ni^{60} at 30.3 MeV.
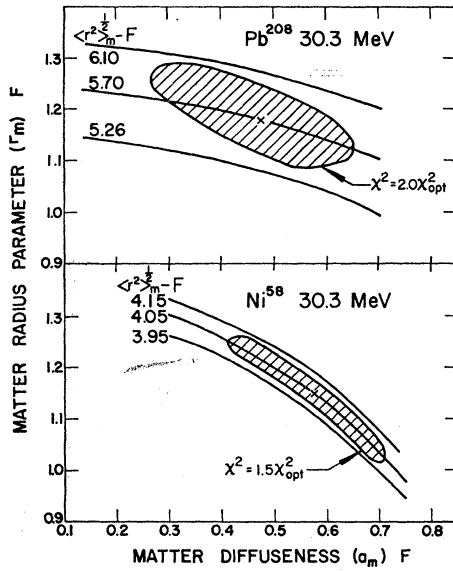
F Fig. 9. Contours of constant best-fit χ^2's for variations of matter-radius (r_m) and -diffuseness (a_m) parameters. The crosses represent the best-fit points. The shaded areas encompass a region within which the fits are visibly indistinguishable. Lines of constant rms matter radius are seen to run nearly parallel to the sides of the shaded areas.

error values. The rms radii and the associated errors obtained for all cases are given in Table IX.

Table IX includes five examples where the rms matter radius has been determined at two or more energies. In all cases the agreement is excellent and indicates the validity of the approximations of the model over the energy range 14.5–40 MeV. The fact that the agreement at different energies in Table IX is better than could be expected for the quoted errors suggests that the method used to obtain the errors from the visual quality of the fits gives an overestimate.

B. Sensitivity to Two-Body Force Range

In the analysis presented thus far the 'direct' part of the nucleon-nucleon force has been taken to have a Yukawa shape and a 2π range. Phenomenological analyses of two-body data clearly show the necessity

of including a hard core in the potential and suggest that the range may be shorter than 2π. Neglecting the hard core will place an upper energy limit of about 100 MeV on the validity of the model. The constancy of the rms matter radii found at different energies in the previous section indicates that no serious error is involved in neglecting the hard core up to energies of 40 MeV and is consistent with the above conclusion.

In order to explore the sensitivity of the model predictions to the two-body force range, the analyses were repeated for a range of values corresponding to $\langle r^2 \rangle_d$ values between 0.01 and 6 F² (a 2π range has a ms radius of 3 F²). The parameters found for Co⁵⁹ at 30 MeV for this range of two-body ms radii are given in Table X. This table shows systematic trends in the parameters with change of $\langle r^2 \rangle_d$ and, in particular, a decrease of $\langle r^2 \rangle_m$ with increasing $\langle r^2 \rangle_d$. However, the ms radius of the folded, real central potential $\langle r^2 \rangle_{RS}$, equal to $\langle r^2 \rangle_m + \langle r^2 \rangle_d$, is remarkably constant over the region of acceptable χ^2's. Clearly, for variations of $\langle r^2 \rangle_d$, the matter parameters are adjusting to maintain the real central potential close to the optimum shape and this term of the potential is dominating the analysis. The geometry of the spin-orbit term of the potential is very closely equal to the matter geometry (Sec. II) so that effects due to this term are not well specified in the data being analyzed. The polarization data are the most sensitive to this term and such data can, in principle, limit the acceptable range of matter radii and, together with differential cross-section data, determine the matter radius and the two-body force range. That this is not so for the present data is illustrated by Fig. 10, where the χ^2 values for cross-section and polarization data are plotted as a function of $\langle r^2 \rangle_d$. Figure 10 shows that, whereas the cross-section curve has a distinct minimum around 2.5 F², the polarization curve is comparatively flat and is doing little to limit the acceptable values for $\langle r^2 \rangle_d$. Clearly, much more accurate polarization data will be needed for this purpose.

However, Fig. 10 can be used to place limits on the value of $\langle r^2 \rangle_d$. The fits for the various $\langle r^2 \rangle_d$ values for all

TABLE IX. Matter rms radii obtained for all the cases considered using a value for $\langle r^2 \rangle_d$ of 3.0 F².

Element	Energy (MeV)	$\langle r^2 \rangle_m^{1/2}$ (F)
Ni⁵⁸	14.5	$3.92_{-0.32}^{+0.23}$
Ni⁵⁸	30.3	$4.05_{-0.07}^{+0.07}$
Ni⁵⁸	40.0	$4.05_{-0.16}^{+0.17}$
Co⁵⁹	30.3	$4.04_{-0.07}^{+0.07}$
Ni⁶⁰	14.5	$4.16_{-0.20}^{+0.09}$
Ni⁶⁰	30.3	$4.09_{-0.05}^{+0.06}$
Zr⁹⁰	14.5	$4.61_{-0.11}^{+0.10}$
Zr⁹⁰	40.0	$4.55_{-0.11}^{+0.17}$
Sn¹²⁰	14.5	$4.95_{-0.18}^{+0.14}$
Sn¹²⁰	30.3	$4.95_{-0.15}^{+0.14}$
Pb²⁰⁸	30.3	$5.69_{-0.31}^{+0.28}$
Pb²⁰⁸	40.0	$5.78_{-0.37}^{+0.34}$

TABLE X. Best-fit parameter sets found in the analysis of 30.3-MeV differential elastic scattering data for Co⁵⁹ using various values of $\langle r^2 \rangle_d$.

$\langle r^2 \rangle_d$ (F²)	0.01	0.75	1.5	3.0	4.5	6.0
V_{RS} (MeV)	47.8	48.3	50.7	55.1	59.9	63.8
W_v (MeV)	0.3	3.1	3.4	4.2	4.1	3.9
W_s (MeV)	7.9	5.2	5.0	4.2	4.3	4.6
r_I (F)	1.217	1.266	1.278	1.360	1.404	1.428
a_I (F)	0.643	0.658	0.645	0.581	0.538	0.507
V_{so} (MeV)	7.0	6.2	5.9	5.7	5.9	6.3
r_m (F)	1.207	1.197	1.182	1.144	1.091	1.041
a_m (F)	0.548	0.622	0.594	0.568	0.570	0.578
$\langle r^2 \rangle_m$ (F²)	17.96	18.37	17.58	16.34	15.28	14.47
$\langle r^2 \rangle_{RS}$ (F²)	17.97	19.12	19.08	19.34	19.78	20.47
χ_σ^2	29.7	11.7	7.5	5.6	9.9	15.7
χ_p^2	33.3	12.6	10.6	9.0	7.4	7.2

cases were examined and, as found previously, these fits got visibly worse when χ^2 increased from the optimum by a factor of 1.5 for medium-weight elements, and by a factor of 2.0 for heavy-weight elements. Using these empirical criteria the optimum value and limits of $\langle r^2 \rangle_d$ were found for all cases. In two cases (Ni[58] and Pb[208] at 40 MeV) the visual quality of the fits was unchanged over the range explored and in these cases no limits could be determined. The results are given in Table XI.

In any individual case in Table XI, the range of $\langle r^2 \rangle_d$ values allowed is quite large (typically 1.0–4.0 F^2) but the optimum values (column 3) show a good measure of agreement. The limits for Ni[58] and Pb[208] at 40 MeV were undetermined but certainly appreciably greater than all other values; these data were neglected and an average $\langle r^2 \rangle_d$ value was obtained from the remaining 10 cases, giving them equal weight. The error in $\langle r^2 \rangle_d$ is difficult to assess since there is clearly a discrepancy between the individual errors and the spread in the optimum values. Using only the variations in the optimum values yields an error in $\langle r^2 \rangle_d$ of 0.10 F^2, whereas using the individual errors of each determination gives 0.6 F^2. These numbers suggest that the individual errors, obtained from the visual fit χ^2 criterion, are overestimated. On the other hand, plots of χ^2 against $\langle r^2 \rangle_d$ such as Fig. 10 suggest that the agreement of the optimum values (column 3, Table XI) is somewhat fortuitous. In the absence of further evidence, the larger error will be taken, yielding a value for $\langle r^2 \rangle_d$ of 2.25±0.6 F^2.

V. ANALYSIS OF PROTON DATA USING CORRECTED $\langle r^2 \rangle_d$

A. Nuclear-Matter Radii

The analysis of Sec. III used a range for the direct part of the nucleon-nucleon force corresponding to a 2π exchange (msr$=3$ F^2). Examination of the sensitivity of the predictions to this choice was made in Sec. IV with the result that a choice of 2.25 F^2 for this range
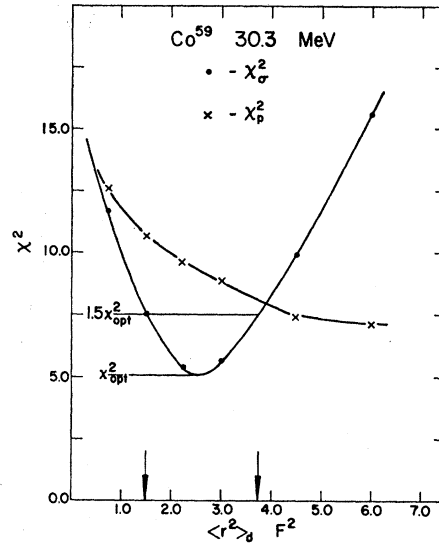

Fig. 10. Variation of best-fit χ^2 values for cross-section and polarization data (Co[59] at 30 MeV) with two-body force msr ($\langle r^2 \rangle_d$).

seems to be more appropriate. In this section the results of a reanalysis of all the data using this new value are presented. It is clear from the results of Sec. IV that the main features of the model will be unchanged by this alteration in $\langle r^2 \rangle_d$ but minor changes in the parameters are to be expected. Table XII gives the parameter sets obtained for the 30.3-MeV data using $\langle r^2 \rangle_d = 2.25$ F^2 and the same procedure as outlined previously for obtaining Table III (3 F^2). A comparison of Tables III and XII confirms that only minor changes in the parameter values have occurred; perhaps the most significant change is that in Table XII (2.25 F^2), the reaction cross sections tend to be less than in Table III (3.0 F^2) and in closer agreement with the experimental values. In particular, the value for Pb[208] is 1986 mb compared to 2047 mb in Table III and an experimental value of 1865±98 mb.

TABLE XI. Optimum values of $\langle r^2 \rangle_d$ for all cases considered together with the range of acceptable values.

Element	Energy (MeV)	Optimum $\langle r^2 \rangle_d$ (F^2)	Upper limit (F^2)	Lower limit (F^2)
Ni[58]	14.5	2.0	5.6	0
Ni[58]	30.3	3.0	5.0	1.2
Ni[58]	40.0	(3.8)	...	...
Co[59]	30.3	2.5	3.8	1.5
Ni[60]	14.5	2.5	4.5	0.6
Ni[60]	30.3	2.0	3.9	0.8
Zr[90]	14.5	2.2	3.6	0.9
Zr[90]	40.0	2.2	4.2	0.7
Sn[120]	14.5	2.4	3.6	1.3
Sn[120]	30.3	2.2	3.5	1.4
Pb[208]	30.3	1.5	4.5	0.4
Pb[208]	40.0	(3.8)	...	...

TABLE XII. Best-fit parameter sets for the 30.3-MeV data using $\langle r^2 \rangle_d = 2.25$ F^2. The analysis procedure was the same as used in obtaining Table III.

Element	Ni[58]	Co[59]	Ni[60]	Sn[120]	Pb[208]
V_{RS} (MeV)	52.53	53.05	52.16	51.13	53.26
W_v (MeV)	4.50	3.84	3.81	3.43	3.45
W_s (MeV)	3.85	4.58	4.71	6.68	6.53
r_I (F)	1.357	1.320	1.311	1.332	1.317
a_I (F)	0.520	0.614	0.609	0.636	0.752
V_{so} (MeV)	5.16	5.75	5.29	5.82	5.49
r_m (F)	1.159	1.162	1.171	1.206	1.206
a_m (F)	0.597	0.579	0.582	0.534	0.497
χ_σ^2	5.47	5.39	4.50	2.97	0.84
χ_p^2	7.78*	9.87*	17.62*	5.58*	3.48*
σ_R (mb)	1085	1153	1154	1643	1986
$\sigma_{R(expt)}$ (mb)	1038±43	1169±39	1053±51	1638±68	1865±98
$\langle r^2 \rangle_m^{1/2}$ (F)	4.12	4.11	4.16	5.02	5.84

TABLE XIII. Best-fit parameter sets for the 14.5-
and 40-MeV data using $\langle r^2 \rangle_d = 2.25$ F².

Element	Ni⁵⁸	Ni⁶⁰	Zr⁹⁰	Sn¹²⁰	Ni⁵⁸	Zr⁹⁰	Pb²⁰⁸
Energy (MeV)	14.5	14.5	14.5	14.5	40.0	40.0	40.0
V_{RS} (MeV)	56.39	55.03	53.57	55.89	49.71	48.77	55.52
W_v (MeV)	...	...	...	...	5.50	5.54	5.69
W_s (MeV)	6.87	9.36	6.92	10.65	2.81	4.21	3.89
r_I (F)	1.353	1.326	1.387	1.267	1.369	1.341	1.467
a_I (F)	0.691	0.569	0.662	0.651	0.541	0.525	0.583
V_{so} (MeV)	6.57	7.01	6.39	6.52	6.05	4.87	5.10
r_m (F)	1.164	1.188	1.221	1.215	1.139	1.197	1.124
a_m (F)	0.492	0.550	0.506	0.539	0.625	0.557	0.736
χ_σ^2	3.60	5.65	3.76	1.13	8.81	24.61	29.13
χ_P^2	6.62	4.22	3.01	2.56	35.05	17.57	6.26
$\langle r^2 \rangle_m^{1/2}$ (F)	3.94	4.14	4.64	5.05	4.13	4.64	5.84

Table XIII gives the parameter sets obtained for the
14.5- and 40.0-MeV data using $\langle r^2 \rangle_d = 2.25$ F². This
table corresponds to Table IV obtained using 3.0 F².
A comparison of Tables XIII and IV shows that, as at
30 MeV, the parameter changes are only of a minor
nature and, in particular, the rms matter radii do not
change by more than the errors of the earlier
determination.

Since the changes occasioned by the reduction of
$\langle r^2 \rangle_d$ from 3.0 to 2.25 F² were relatively small it was not
considered necessary to repeat the extensive explora-
tion of the parameter space which is described in
Sec. IV for the 3.0 F² case. For the remainder of this
paper the results obtained using 2.25 F² will be used;
however, the errors on these results are those obtained
from the investigation of Sec. IV, using 3.0 F².

The final values for the nuclear rms matter radii,
determined in this analysis, are listed in Table XIV.

B. Volume Integrals

The form of the model used in the present analysis
involves the assumptions concerning ρ_p, ρ_n, and u_r

given by Eq. (33). These lead to Eq. (37),

$$J_{RS}/A = J_d + \zeta J_d (N-Z)/A ,$$

where

$$J_{RS} = -\int U_{RS}(r)d\mathbf{r} \quad \text{and} \quad J_d = -\int u_d(\eta)d\eta .$$

The values of J_{RS} are readily determined from the
present analysis, being simply the volume integrals of
the real central potential associated with the parame-
ters of Tables XII and XIII. These volume integrals
divided by A are listed in Table XV.

A plot of J_{RS}/A against $(N-Z)/A$ for all elements at
a given energy gives an intercept J_d and a slope ζJ_d.
Results for the three energies examined are shown
separately in Fig. 11, where the values of J_d are also
given. It is seen that the values of J_d, ranging from
425 ± 25 to 380 ± 20 MeV F³ between 14.5 and 40 MeV,
are nearly independent of energy and are in good agree-
ment with the value of 422 MeV F³ obtained in Sec.
II B from the α-α analysis of Ali and Bodmer[13] and the
value of 400 MeV F³ obtained from the nucleon-
nucleon potential of Eq. (25). This indicates that, for
the cases considered here, the antisymmetrization and
polarization effects do not play an important role in
the interaction, in agreement with the conclusion
reached by Drell.[10] The slight tendency for the intercept
(J_d) to decrease with energy can be interpreted as due
to second-order effects which are ignored in the present
model. In particular, since the polarization effect is ex-
pected to become less important as energy increases,
the gradual decrease in J_d with energy could have been
anticipated.

The errors shown on the points in Fig. 11 are obtained
from the variations in the volume integrals found from
the parameters determined for the a_m grids of Sec. IV
(e.g., Fig. 8) using the empirically determined 1.5
χ_{opt}^2 criterion (2.0 χ_{opt}^2 for heavy elements). Although

TABLE XIV. Matter, proton, and neutron central densities and rms radii. The matter data are obtained from the parameters of
Tables XII and XIII and the proton data are deduced from the results of Acker et al.[a] In computing the errors, any error in the proton
data has been neglected.

Element	Energy (MeV)	$\langle r^2 \rangle_m^{1/2}$ (F)	$\langle r^2 \rangle_p^{1/2}$ (F)	$\langle r^2 \rangle_n^{1/2}$ (F)	Average $\langle r^2 \rangle_n^{1/2} - \langle r^2 \rangle_p^{1/2}$ (F)	ρ_{m0} (nucleons F⁻³)	ρ_{p0} (protons F⁻³)	ρ_{n0} (neutrons F⁻³)
Ni⁵⁸	14.5	$3.94_{-0.23}^{+0.23}$	3.74	$4.12_{-0.62}^{+0.44}$	0.71 ± 0.14	0.136 ± 0.012	0.076	0.060 ± 0.012
	30.3	$4.12_{-0.07}^{+0.07}$		$4.45_{-0.14}^{+0.14}$		0.131 ± 0.016		0.055 ± 0.016
	40.0	$4.13_{-0.16}^{+0.17}$		$4.47_{-0.31}^{+0.33}$		0.135 ± 0.017		0.059 ± 0.017
Co⁵⁹	30.3	$4.11_{-0.07}^{+0.06}$	3.75	$4.39_{-0.13}^{+0.11}$	0.64 ± 0.12	0.131 ± 0.015	0.072	0.059 ± 0.015
Ni⁶⁰	14.5	$4.14_{-0.20}^{+0.09}$	3.77	$4.44_{-0.37}^{+0.17}$	0.70 ± 0.10	0.125 ± 0.012	0.073	0.052 ± 0.012
	30.3	$4.16_{-0.06}^{+0.06}$		$4.47_{-0.09}^{+0.11}$		0.128 ± 0.014		0.055 ± 0.014
Zr⁹⁰	14.5	$4.64_{-0.11}^{+0.10}$	4.22	$4.94_{-0.20}^{+0.18}$	0.72 ± 0.20	0.121 ± 0.019	0.071	0.050 ± 0.019
	40.0	$4.64_{-0.11}^{+0.17}$		$4.95_{-0.20}^{+0.30}$		0.126 ± 0.019		0.055 ± 0.019
Sn¹²⁰	14.5	$5.05_{-0.18}^{+0.14}$	4.59	$5.36_{-0.31}^{+0.24}$	0.67 ± 0.20	0.123 ± 0.016	0.066	0.057 ± 0.016
	30.3	$5.02_{-0.16}^{+0.14}$		$5.30_{-0.25}^{+0.24}$		0.126 ± 0.012		0.060 ± 0.012
Pb²⁰⁸	30.3	$5.84_{-0.31}^{+0.28}$	5.44	$6.08_{-0.57}^{+0.46}$	0.64 ± 0.40	0.130 ± 0.016	0.063	0.067 ± 0.016
	40.0	$5.84_{-0.37}^{+0.34}$		$6.08_{-0.61}^{+0.56}$		0.150 ± 0.018		0.087 ± 0.018

[a] Reference 32.

TABLE XV. Volume integrals (J_{RS}) of the real central potential, divided by A, for all cases (Tables XII and XIII) using $\langle r^2 \rangle_d = 2.25$ F². (The errors are obtained from the a_m grids using $\langle r^2 \rangle_d = 3.0$ F²).

Element	Energy (MeV)	J_{RS}/A (MeV F³)
Ni⁵⁸	14.5	421±16
	30.3	409±20
	40.0	377±15
Co⁵⁹	30.3	411±10
Ni⁶⁰	14.5	445±11
	30.3	413±10
Zr⁹⁰	14.5	445±23
	40.0	390±11
Sn¹²⁰	14.5	454±10
	30.3	406± 8
Pb ²⁰⁸	30.3	411±12
	40.0	371±14

$\langle r^2 \rangle_d = 3.0$ F² was used in Sec. IV whereas 2.25 F² is used here, this should have a negligible effect on the error values. It is clear from Fig. 11 that the slopes of the curves are not well determined and ζ is limited only to the range +1.0 to −0.5. Hence it is not possible to determine this quantity with any accuracy from existing proton elastic scattering data. Because of this, no attempt was made to include corrections due to the change of Coulomb potential with Z. The best value for ζ is obtained as in Sec. II B from the coefficients of the terms of the two-body potential [Eq. (35)].

The volume integrals found here, and their dependence on $(N-Z)/A$ and E, are analogous to the corresponding variations of the real central strength of the standard optical model. Such variations in the standard optical model are only apparent when the assumptions are made that the diffuseness parameter is constant and the radius parameter has an $A^{1/3}$ variation. An advantage of the present model is that these assumptions are avoided and the optimum parameter sets are used to deduce geometrical and strength information. The variations with $(N-Z)/A$ and E found here are consistent with those found in the standard optical model but the relatively unique values found in the latter case are a feature introduced by making geometrical assumptions and are not otherwise well-defined by the data.

VI. NEUTRON DISTRIBUTIONS

It is of interest to compare the rms matter radii obtained here with corresponding proton values obtained from muonic x-ray and electron scattering measurements. Such measurements were not available for the isotopes analyzed in the present work so interpolated values were used. The results of Acker et al.[32] for nuclear-charge distributions are well represented

[32] H. A. Acker, G. Backenstoss, C. Daum, J. C. Sens, and S. A. Dewitt, Nucl. Phys. **87**, 1 (1966).
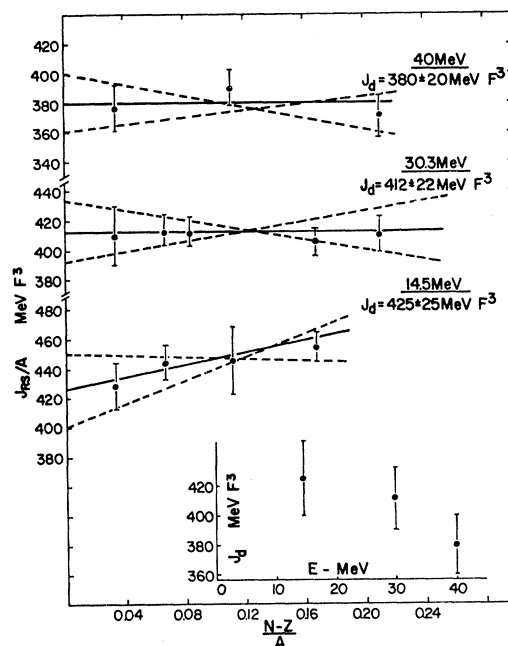

FIG. 11. Variation of J_{RS}/A with $(N-Z)/A$ for the 14.5-, 30.3-, and 40.0-MeV analyses. The intercept at $(N-Z)/A = 0$ gives a value for J_d. The inset shows the variation of J_d with energy.

($A = 50$–120) by a Saxon-Woods shape

$$[1 + \exp((r - R_{ch})/a_{ch})]^{-1},$$

with

$$a_{ch} = 0.502 \text{ F}$$

and

$$R_{ch} = (1.106 + 1.05 \times 10^{-4}A)A^{1/3} \text{ F}.$$

To obtain nuclear-proton distributions from these charge distributions a correction is necessary for the finite size of the proton. The major effect of unfolding the proton size is to reduce the falloff distance of the distribution and leave the halfway radius almost unchanged. The msr of the proton was taken to be 0.6 F² and the correction was made by taking the proton halfway radius, $R_p = R_{ch}$, and obtaining a_p from the relation $\langle r^2 \rangle_{ch} = \langle r^2 \rangle_p + 0.6$. This gives $a_p = 0.454$ F for all A.

Using the matter parameters from Tables XII and XIII and the proton parameters given above, the corresponding neutron distributions and their rms radii are readily calculated. The rms radii are given in Table XIV. It is also of interest to compare the central densities of the matter, proton, and neutron distributions ρ_{m0}, ρ_{p0}, and ρ_{n0}. These are included also in Table XIV.

It is seen from Table XIV that the nuclear-matter rms radii obtained here are significantly greater than the proton values obtained from nuclear-charge measurements and hence that the neutron distributions extend beyond those of the protons. This result is in contradiction to the assumption made in Sec. III that

$\rho_p(r)/\rho_n(r) = Z/N$. This assumption was introduced to simplify the computation and is in no way essential to the model. Its introduction yields a volume shape for the isospin part of the central potential, whereas the present results indicate that it is surface-peaked. The error involved is not serious since the isospin term is small compared to the main real central term (approximately 10% for Pb^{208}, the worst case). It will, however, have the effect of producing slightly too large a value for the matter rms radii obtained here. A second simplification used in the present analysis was to use only the first term of the expression for the spin-orbit potential. The error involved due to this is small but also tends to give too large values for the rms matter radii. The extent of these errors has been estimated and in all cases they prove to be less than the quoted errors of the measurement. In the worst case (Pb^{208}) the matter rms radius could be as much as 0.2 F too large, with a quoted error of about 0.3 F.

Although the simplifying assumptions used here produce only a small overestimate of the matter rms radii it becomes significant when differences between neutron and proton rms radii are examined. Thus for Pb^{208} a value for this difference of 0.64±0.40 F is given in Table XV and this could be overestimated by as much as 0.33 F. Since these assumptions were only for computational simplicity they can readily be removed and the complete expression of Sec. II [Eqs. (15)–(17)] used such calculations are not included in this paper. It should be emphasized that the values quoted here for the overestimate of the rms matter radius for Pb^{208} are

upper limits for the worst case; these upper limits are much less for the lighter nuclei and the error could well be unimportant, even for the n-p rms radius difference, in all cases.

It is noticeable in Table XIV that the neutron-proton rms radius difference (column 6) is constant, within the errors, for all the nuclei examined and that the central density remains remarkably constant (column 7). The proton central density derived from nuclear-charge measurements decreases with A; combining this with the present matter results leads to the central neutron density increasing with A and the neutron edge falloff distance decreasing markedly with A. The proton and neutron central densities become equal, within the limits of accuracy, in the heavy nuclei. These features are illustrated in Fig. 12, where the density distributions are plotted for four cases from Ni^{58} to Pb^{208}.

VII. IMAGINARY POTENTIAL

The considerations given here so far have concerned only the relationship of the real parts of the optical-model potential to each other and to physically significant quantities; the imaginary part of the potential has been used with its normal parametrization. The imaginary potential represents, in a simple form, the effects of all reaction channels other than the elastic channel and must be inherently very complicated. However, since the simple phenomenological parametrization of this term, used both here and in the standard optical-model treatment, does in fact enable a good representation of elastic-scattering data to be made, it is reasonable to hope that the phenomenological forms found can be derived, at least in gross features, from an approximate description of the physical processes involved.

One basic difficulty of such an approach lies in the fact that relatively severe ambiguity problems are often found in the four parameters used to define the phenomenological imaginary potential. An example of such problems is the case of Ni^{58} at 30.3 MeV discussed in Sec. III (Fig. 1.) This means that the form found in the analysis may not be the optimum form but one that gives an equivalent or an almost equivalent fit to the particular set of data analyzed. However, two features of the phenomenological imaginary potential seem to be always present for protons of incient energies considered here: (1) a surface peaking, and (2) the tail-region half-maximum point lies at a significantly larger radius than the halfway point of the real central potential. Where ambiguities have been explored, the various imaginary potentials, giving satisfactory fits, tend to have similar radial variations in the surface region. It is the purpose of the present section to show that these features of the imaginary potential are reproduced from relatively simple considerations.
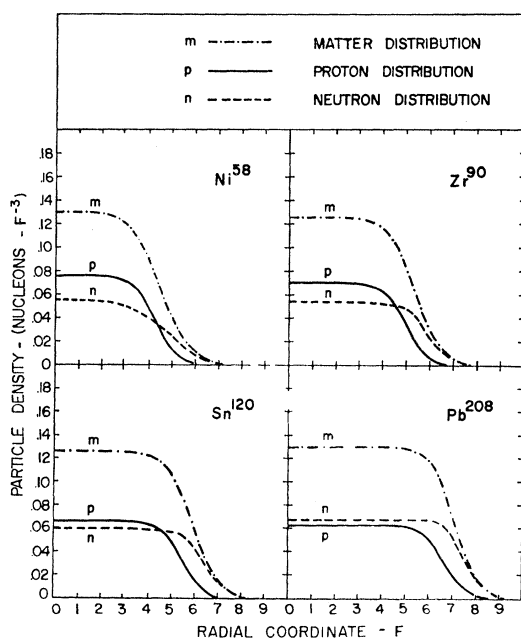

FIG. 12. Plots of the radial variations of matter, proton, and neutron densities for various elements.

Several authors[33-36] have used a semiclassical method which enables the proton imaginary potential to be written as

$$W(r) = \tfrac{1}{2} h v_p [\rho_n(r)\langle\sigma_{pn}\rangle + \rho_p(r)\langle\sigma_{pp}\rangle], \quad (46)$$

with v_p being the velocity of the incident proton at the position where the imaginary potential is evaluated. The quantities $\langle\sigma_{pn}\rangle$ and $\langle\sigma_{pp}\rangle$ are average proton-neutron and proton-proton cross sections, with the average taken in an appropriate fashion over all possible values of the relative collision momentum under the restrictions imposed by the Pauli exclusion principle. In the present work these averages are obtained using the following simplifying assumptions:

(1) The momentum distribution of the nucleons in the nucleus is given by a Fermi-gas model with

$$k_{Fi}^3 = 3\pi^2 h^3 \rho_i(r), \quad (47)$$

where the subscript i denotes either p (proton) or n (neutron);

(2) the free nucleon-nucleon differential cross section in the c.m. system is assumed to be isotropic; and

(3) the nucleon-nucleon total cross section is given by

$$\sigma_{pi} = A_i/(B_i + E_0), \quad (48)$$

with E_0 being the energy in the c.m. system and

$A_n = 4.32$ MeV b, $B_n = 0.54$ MeV,

$\quad A_p = 1.55$ MeV b, $B_p = 0.85$ MeV. (49)

The assumption of isotropic angular distributions will underestimate the cross sections in the forward and backward regions and overestimate the cross sections at other angles. Since forward and backward scatterings in the nucleus are restricted by the exclusion principle, this assumption will cause an overestimate of W and this overestimate will be particularly severe in the regions of higher density. The energy dependence of assumption (3) gives a fair representation of the data up to c.m. energies of about 70 MeV[37] and probably injects no significant error into the calculation of W.

With these assumptions, it is straightforward to show that[38]

$$\langle\sigma_{pi}\rangle = 3pmA_i F_{pi}/k_{Fi}^3, \quad (50)$$

where

$$F_{pi} = \int \frac{x(1+x^2-\alpha_i^2)}{[2(1+x^2+\xi_i)]^{1/2}}$$

$$\times \ln\frac{(1+3x^2+2\xi_i)+2x[2(1+x^2+\xi_i)]^{1/2}}{(1+3x^2+2\xi_i)-2x[2(1+x^2+\xi_i)]^{1/2}}dx, \quad (51)$$

[33] A. M. Lane and C. F. Wandel, Phys. Rev. **98**, 1524 (1955).
[34] K. Harada and N. Oda, Progr. Theoret. Phys. (Kyoto) **21**, 260 (1959).
[35] M. L. Goldberger, Phys. Rev. **74**, 1269 (1948).
[36] E. Clementel and C. Villi, Nuovo Cimento **1**, 176 (1955).
[37] W. N. Hess, Rev. Mod. Phys. **30**, 368 (1958).
[38] This expression was obtained by Clementel and Villi (Ref. 36). The present formulation is an extension of their work to the case of a finite nucleus.

with p being the momentum of the incident proton and m being the nucleon mass. Also, the definitions of x, α_i^2, and ξ_i are

$$x = k/p,$$
$$\alpha_i^2 = x_{Fp}^2 + x_{Fi}^2, \quad (52)$$
$$\xi_i = mB_i/p^2,$$

with k being the momentum of the target nucleon and x_{Fi} given by

$$x_{Fi} = k_{Fi}/p. \quad (53)$$

For the integral in Eq. (51), the limits of integration are

$$x_{Fi}^2 > x^2 > 0 \quad \text{for} \quad \alpha_i^2 \leq 1 \quad (54)$$

and

$$x_{Fi}^2 > x^2 > \alpha_i^2 - 1 \quad \text{for} \quad \alpha_i^2 \geq 1. \quad (55)$$

To evaluate these expressions, the momentum p at position r was calculated using the real central and Coulomb potentials found for the corresponding best-fit set parameters (Tables XVI and XIII) together with the proton and neutron density distributions obtained as in Sec. VI. The imaginary potential W is then readily obtained from Eq. (46). This radial variation of W is to be compared with the phenomenological imaginary potentials given by the parameters of Tables XIII and XIV.

The comparison for Ni^{58} at the three energies analyzed is given graphically in Fig. 13. To facilitate the shape comparison, the phenomenological curves of Fig. 13 have been normalized to the calculated curves to make the surface peak heights the same. It is clear
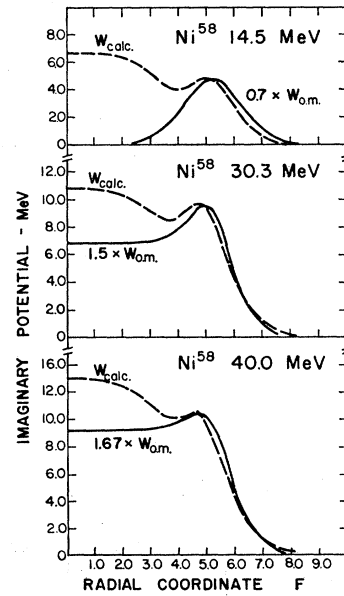

FIG. 13. Comparison of radial variation of the imaginary potential for Ni^{58} at 14.5, 30.3, and 40 MeV, obtained (1) phenomenologically (W_{om}) and (2) by calculation from nucleon-nucleon cross-section data (W_{calc}, see text). The phenomenological curves have been normalized to make the surface peak heights equal.

from Fig. 13 that the surface shapes of the imaginary potential are being well reproduced by the calculation. The 30.3- and 40.0-MeV predictions are higher than the phenomenological values. This was anticipated from the use of assumption (2) and qualitatively is as expected, being worse for the central high-density regions. The extent of the correction involved because of this assumption of isotropy is not readily calculated, but could be as high as 50%.[39] In the 14.5-MeV case of Fig. 13, the predicted values of W are less than the phenomenological ones but here only a surface form was used in the model fitting whereas a volume component is also predicted. A pure surface form was used for the phenomenological W at 14.5 MeV since this involved the minimum number of parameters needed to represent the data. A form closer to the calculated one could well give equally satisfactory fits. The calculations, although relatively crude, give a clear indication that the number of parameters used for W in the model can be reduced from the present four to perhaps one or two.

The ambiguity problems normally found for the phenomenological W suggest that a better approach would be to analyze the data using the predicted form and explore the adjustments required to obtain an equally good fit to the data. It was felt that such an approach was not justified until a more sophisticated treatment of the angular dependence of the nucleon-nucleon scattering has been included in the calculations.

The surface peaking obtained in the calculations presented here is found only to be present because of the greater radial extent of the neutron distribution compared to the proton distribution. For ρ_p proportional to ρ_n no significant surface peaking is found.[40] The surface peaking for W, always found phenomenologically for protons of these energies, can thus be attributed to the presence of excess neutrons in the nuclear surface and as supporting evidence for the results presented here. It should be pointed out that a consequence of these features is that the position of the surface peak is sensitive to the rms radius difference of the neutron and proton distribution and, since relatively large errors are found here for this difference (typically 0.1–0.4 F), using a calculated, self-consistent shape for W might place added restrictions on the allowed variations of the matter msr obtained from the model and thus yield a more accurate value of $\langle r^2 \rangle_m$.

VIII. DISCUSSION

The reformulation of the optical model developed here has proved to be quite successful in its application. The simplest measure of this success lies in the fact that the quality of fit to elastic proton data is maintained or improved with two fewer parameters than are normally needed (Tables V and VI). More significant, however, is the physical understanding of the model parameters associated with the reformulation. Proton elastic scattering measurements of good accuracy can now be used to obtain information about nuclear-matter distributions; only limited information is at present available concerning these quantities from other sources. Information can also be obtained concerning the strength and msr of the direct component of the two-body force.

A. Matter Radii

Tables VII and VIII together with Fig. 9 demonstrate clearly that a good measure of the nuclear rms matter radius can be extracted from the analysis by obtaining a reasonable fit to the data and that $\langle r^2 \rangle_m$ is a well-defined quantity, relatively insensitive to the details of the parameters used and the quality of the fitting. This result is in sharp contrast to the behavior of the radius and diffuseness matter parameters, which can vary over wide limits (Fig. 9). The elastic scattering of protons at energies below 50 MeV is largely determined by the surface region of the nucleus and since the mean-square matter radius emphasizes this region its constancy is to some extent not unexpected. Nevertheless, it is somewhat surprising that $\langle r^n \rangle_m$ should be so well defined for any value of n; the significance of this result is not completely understood.

One particularly satisfactory feature of the results is the agreement between the rms matter radii obtained for the same element at different energies (Table XIV). This consistency suggests that no serious errors are involved in the approximations used in the formulation of the model. The agreement found for the rms radii in Table XIV is much better than might be anticipated on the basis of the error assignments. This indicates that the method used to obtain these errors yields an overestimate. It is, however, not clear how these errors can be reduced on an objective basis.

The comparison of the rms matter radii found here with the rms proton radii obtained in other ways indicates clearly that the matter radii are bigger than the proton values for the same element. This implies that neutron distributions are more extended than proton distributions in nuclei. Such a possibility has been recognized for a long time but only limited evidence for the difference has previously been available.[41] It has been pointed out that studies of K^--meson absorption should be sensitive to the ratio of protons to neutrons in the nuclear surface.[42] Measurements[43] of K^--meson interactions in nuclear emulsions have recently been

[39] G. C. Morrison, H. Muirhead, and P. A. B. Murdock, Phil. Mag. **44**, 795 (1955).
[40] This result is contrary to the earlier result by Harada and Oda (Ref. 34) due, probably, to the difference in the real potential depths used in the two calculations.

[41] M. H. Johnson and E. Teller, Phys. Rev. **92**, 801 (1953).
[42] P. B. Jones, Phil. Mag. **3**, 33 (1958); D. H. Wilkinson, in *Proceedings of the Conference on Nuclear Structure*, edited by D. A. Bromley and E. W. Vogt (University of Toronto Press, Toronto, Canada, 1960), p. 20.
[43] D. H. Davis, S. P. Lovell, M. Csejthey-Barth, J. Sacton, G. Schorochoff, and M. O'Reilly, Nucl. Phys. **B1**, 434 (1967).

analyzed by Burhop[44] and indicate a difference of neutron and proton rms radii of about 0.5 F for Ag. This value is in good agreement with the results of Table XIV. Further evidence that the differences found here are reasonable is obtained from a bound-state calculation by Kallio[45] in which the binding energies for the last neutron and proton in Pb^{208} were fitted by adjusting the shell-model well parameters and the msr for neutrons and protons were computed from the wave functions. The difference between the rms radii for neutrons and protons was insensitive to the details of the well parameters so long as the binding energies were correctly given, and had a value of about 0.3 F, in reasonable agreement with the value 0.64±0.40 F of Table XIV.

Recently, results have become available for the charge distributions of a number of Ca isotopes[46] and shell-model calculations have been made by several authors to obtain an understanding of the variations found.[47] As was the case for the Pb^{208} calculation mentioned above, such calculations do not include any connection between the geometry of the shell-model potentials used and the proton and neutron distributions predicted from the wave functions. However, with reasonable assumptions concerning the isobaric variation of the well depth, the analyses indicate a greater ms radius for neutrons compared to protons. Similar calculations using Coulomb energy differences, obtained from measurements of isobaric analog states, suggest the same effect.[48] In contrast to this evidence supporting the present results, the early measurements of π^+, π^- scattering from Pb^{208} indicated the neutron and proton distributions to be the same.[49]

The present work used interpolated values for the proton radii since measurements of the particular isotopes analyzed here were not available. Clearly, as such measurements are made and the corresponding matter radii obtained with greater accuracy along the lines developed here, a much more detailed investigation of nuclear radii will be possible. Of particular interest will be a study of the variations within an isobaric sequence and of the feature, found here, of an approximately constant n-p rms radius difference for all medium and heavy nuclei.

B. Nucleon-Nucleon Force Data

The analysis yields information on the range and the volume integral of the spin-isospin–independent part of the nucleon-nucleon potential. The values found for the msr from the analysis of data for various elements and at various energies are in good agreement with each other (Table XI). This agreement is much better than could be expected from the estimated errors in the individual determinations and is an indication that these errors are overestimates. It is clear from Fig. 10 that the existing polarization measurements are placing no significant constraints on the value of $\langle r^2 \rangle_d$. In the present simplified presentation, in which only the first term of the spin-orbit folding series is used, the difference in the msr of the real and spin-orbit geometries is attributed entirely to this direct component of the nucleon-nucleon force. When this simplification is removed, the difference in the msr will still be dominated by the same two-body force component so that polarization data of significantly greater accuracy should enable a better determination of $\langle r^2 \rangle_d$ to be made. The volume integral of the direct component of the nucleon-nucleon force (J_d) shows a tendency to decrease with incident proton energy although the results are consistent with no energy dependence (Fig. 11).

Various forms have been used successfully for two-body potentials to obtain a fit to nucleon-nucleon scattering data. These potentials use a repulsive core when high-energy data is included in the fitting. Such effects were neglected in the present work and a pure Yukawa form was used. However, the tail of the force used here should agree with that found in fitting nucleon-nucleon data and it is reasonable to compare the present msr with that of the corresponding attractive components of the nucleon-nucleon potentials. Thus, Gammel and Thaler,[50] using a Yukawa shape, have quoted singlet and triplet msr of 2.9 and 1.4 F^2, respectively, indicating that the msr of u_d is around 2 F^2. A nucleon-nucleon potential which has been used successfully in several bound-state calculations of light nuclei by Tang et al.[51] uses an exponential form for the attractive part with a msr for the direct component of about 2.5 F^2. An alternative approach to obtain the range of this component of the force was used by Ali and Bodmer,[13] who made a detailed analysis of α-α scattering which yields a value for $\langle r^2 \rangle_d$ of 2.51±0.40 F^2. These three values for the msr of the direct component of the nucleon-nucleon force are all in good agreement with the value of 2.25 F^2 found here.

It is also noteworthy that the value of the volume integral J_d obtained here agrees very well with that for the two-body potential of Eq. (25). This latter potential has been used in a number of resonating-group calculations involving light nuclei, and, in all these cal-

[44] E. H. S. Burhop, Nucl. Phys. **B1**, 438 (1967).

[45] A. Kallio (private communication).

[46] K. J. Van Oostrum, R. Hofstadter, G. K. Noldeke, M. R. Yearian, B. C. Clark, R. Herman, and D. G. Ravenhall, Phys. Rev. Letters **16**, 528 (1966).

[47] F. G. Perey and J. P. Schiffer, Phys. Rev. Letters **17**, 324 (1966); B. F. Gibson and K. J. Van Oostrum, Nucl. Phys. **A90**, 159 (1957); A. Swift and L. R. B. Elton, Phys. Rev. Letters **17**, 484 (1966); Nucl. Phys. **A94**, 52 (1967).

[48] J. A. Nolen, Jr., J. P. Schiffer, N. Williams, and D. Von Ehrenstein, Phys. Rev. Letters **18**, 1140 (1967).

[49] A. Abashain, R. Cool, and J. W. Cronin, Phys. Rev. **104**, 855 (1956). *Note added in manuscript.* It has been brought to our attention that a later analysis of this data [L. R. B. Elton, Rev. Mod. Phys. **30**, 557 (1958)] concluded that $\langle r^2 \rangle_m^{1/2}$ exceeds $\langle r^2 \rangle_p^{1/2}$ by approximately 0.3 F, in good agreement with the present work.

[50] K. A. Brueckner and J. Gammel, Phys. Rev. **109**, 1023 (1958).

[51] Y. C. Tang, E. W. Schmid, and R. C. Herndon, Nucl. Phys. **65**, 203 (1965); E. W. Schmid, Y. C. Tang, and K. Wildermuth, Phys. Letters **7**, 263 (1963).

culations, good agreement with experimental data on scattering cross sections has been obtained.[52]

C. Imaginary Potential

The relatively crude calculation of the imaginary potential, described in Sec. VII, proved quite successful in reproducing the surface shape of the phenomenological form found in the main analysis. The agreement between the calculated and the phenomenological imaginary potentials in the central regions of the nucleus will certainly be improved by a better calculation along the present lines. It is probable that the shape obtained from a more refined calculation will be able to give as good a fit to the experimental data as is achieved with the present phenomenological shape. Thus the geometries of all the terms of the optical-model potential, at least in the surface region, have been shown to be related to the nuclear neutron and proton distributions by the application of relatively simple physical principles.

D. Approximations of the Model

As developed, the model gives a first-order treatment of the problem. The analysis of data given here involved two additional simplifications regarding the treatment of the isospin- and spin-orbit terms. These simplifications involve only small errors (Sec. VI) and are readily removed at the expense of longer computational periods. The internal consistency of the present results of the analysis indicate clearly that no effects of major importance have been neglected. Particularly reassuring are (1) the close agreement between the nuclear-matter radii found for the same element at different energies, (2) the constancy of $\langle r^2 \rangle_d$ for the various cases, and (3) the relatively slow variation of J_d with energy. This implies that second-order effects are playing only a minor part since any larger contribution would almost certainly result in an energy dependence of the geometrical results and a pronounced energy dependence for the strength of the force. Nevertheless, it is possible that the results found here are to some extent fortuitous and it is important to investigate, as far as possible, the effects of including (1) core polarization, (2) a repulsive core in the nucleon-nucleon potential, and (3) the antisymmetrization of the incident particle with the target nucleons. The present work suggests that these effects will only modify the potential near the origin; the absorptive component needed in the analysis of proton elastic scattering data at these energies makes the results insensitive to the interior region.

[52] D. R. Thompson and Y. C. Tang, Phys. Rev. **159**, 806 (1967); Phys. Rev. Letters **19**, 87 (1967).

E. Applicability of the Model

The expressions obtained for the real parts of the potential in Sec. II were based on the assumption of scattering from spin-zero nuclei. One of the cases studied (30-MeV proton elastic scattering from Co^{59}) does not fall into this category. However, no features were found in the cobalt analysis which were not present for the other elements, indicating that the model is more generally applicable than is implied by the formulation given. The full extent of this applicability has yet to be determined.

The analysis given here shows the model to be valid over a proton energy range from 14–40 MeV. There will be a lower limit of applicability caused by the onset of sizeable polarization effects; it seems probable that this limit, in itself, will be unimportant since it is likely that other effects such as resonance phenomena and compound elastic contributions will already have severely limited the use of a potential description of the interaction. An upper energy limit of applicability will be reached when hard-core effects can no longer be neglected. This limit is likely to be somewhere in the energy range 60–100 MeV.

The model has been applied here only to the analysis of proton elastic scattering data. It is clearly immediately applicable to neutron elastic scattering data and is readily extended to the analysis of the elastic scattering of complex particles by nuclei. An additional assumption required in these latter cases is that the projectile does not become appreciably polarized during the interaction. In cases where this can be reasonably assumed, the real parts of the potential can be obtained by a double-folding procedure. An attractive feature of analyzing data in this way is that the potentials derived from data obtained with different projectiles are directly connected in an unambiguous way if a reasonable spatial wave function is available for each projectile. Such analyses will constitute a good test of the ideas presented here.